

X-ray Absorption by the Low-redshift Intergalactic Medium: A Numerical Study of the Λ CDM model

Xuelei Chen¹

Department of Physics, The Ohio State University, Columbus, OH 43210, USA

David H. Weinberg

Department of Astronomy, The Ohio State University, Columbus, OH 43210, USA

Neal Katz

Department of Astronomy, University of Massachusetts, Amherst, MA 01003, USA

Romeel Dave²

Steward Observatory, University of Arizona, Tucson, AZ 85721, USA

ABSTRACT

Using a hydrodynamic simulation of a cold dark matter universe with a cosmological constant (Λ CDM), we investigate the “X-ray forest” absorption imprinted on the spectra of background quasars by the intervening intergalactic medium (IGM), at redshift $z \approx 0$. In agreement with previous studies, we find that O VII and O VIII produce the strongest absorption features. The strong oxygen absorbers that might be detectable with *Chandra* or *XMM-Newton* arise in gas with $T \sim 10^{5.5}$ K – $10^{6.5}$ K and overdensities $\delta \gtrsim 100$ that are characteristic of galaxy groups. Future X-ray missions could detect weaker oxygen absorption produced by gas with a wider range of temperatures and the lower densities of unvirialized structures; they could also detect X-ray forest absorption by carbon, nitrogen, neon, iron, and possibly silicon. If the IGM metallicity is $Z = 0.1Z_{\odot}$, as we assume in most of our calculations, then the predicted number of systems strong enough for a $\sim 5\sigma$ detection with *Chandra* or *XMM-Newton* is extremely low. However, scatter in metallicity increases the number of strong absorbers even if the mean metallicity remains the same, making the predictions somewhat more optimistic. Our simulation reproduces the high observed incidence of O VI (1032Å, 1038Å) absorbers, and the most promising strategy for finding the X-ray forest is to search at the redshifts of known O VI systems, thus reducing the signal-to-noise threshold required for a significant detection. However, while many O VI absorbers have associated O VII

¹Present address: Institute for Theoretical Physics, U.C. Santa Barbara, Santa Barbara, CA 93106, USA

²Hubble Fellow

or O VIII absorption, the O VI systems trace only the low temperature phases of the X-ray forest, and a full accounting of the strong O VII and O VIII systems will require a mission with the anticipated capabilities of *Constellation-X*. The large effective area of the *XEUS* satellite would make it an extremely powerful instrument for studying the IGM, measuring X-ray forest absorption by a variety of elements and revealing the shock-heated filaments that may be an important reservoir of cosmic baryons.

Subject headings: cosmology: large-scale structure of universe — cosmology: theory — intergalactic medium — numerical method — quasars: absorption lines — X-rays: general

1. Introduction

The primordial deuterium abundance, combined with the theory of big bang nucleosynthesis, implies a cosmic baryon density $\Omega_b \approx 0.02h^{-2}$ (Burles & Tytler 1997, 1998; here $h \equiv H_0/100 \text{ km s}^{-1}\text{Mpc}^{-1}$), in agreement with recent estimates from the cosmic microwave background anisotropy measurements (de Bernardis et al. 2002; Spergel et al. 2003). This value is an order of magnitude higher than the estimated density of stellar mass (e.g., Fukugita, Hogan, & Peebles 1998). At redshifts $z \sim 2 - 4$, it appears that most baryons reside in the diffuse, photoionized intergalactic medium (IGM) that produces the Ly α forest: that is what hydrodynamic simulations predict (Cen et al. 1994; Zhang, Anninos, & Norman 1995; Hernquist et al. 1996; Miralda-Escudé et al. 1996; Theuns et al. 1998), and it is what the measured opacity of the Ly α forest implies given reasonable estimates of the neutral fraction (Rauch & Haehnelt 1995; Hernquist et al. 1996; Rauch et al. 1997; Weinberg et al. 1997b; Schaye 2001). By low redshift, according to the simulations, some of this gas makes its way into galaxies and some remains in a diffuse photoionized medium at $T \sim 10^4 \text{ K}$, but a significant fraction is shock-heated to higher temperatures (Cen & Ostriker 1999a; Davé et al. 1999). Cen & Ostriker (1999a) coined the term “warm-hot intergalactic medium” (WHIM) to refer to intergalactic gas in the temperature range $10^5 \text{ K} < T < 10^7 \text{ K}$, and a variety of numerical simulations predict that 30-40% of baryons reside in the WHIM at $z = 0$ (Davé et al. 2001).

While the hot ($T \sim 10^7 - 10^8 \text{ K}$), dense ($\delta \equiv \rho/\bar{\rho}_b > 100$) gas in galaxy clusters can be readily detected in X-rays, most of the shocked IGM lies at lower temperatures and densities, where its X-ray emission is relatively feeble. One of the few prospects for observing this component is via the X-ray *absorption* that its highly ionized metal lines would produce in the spectra of background quasars. The absence of continuous “X-ray Gunn-Peterson” absorption provided early limits on the density and temperature of the IGM (Shapiro & Bahcall 1980; Aldcroft et al. 1994). Anticipating the high spectroscopic resolution of Chandra and XMM-Newton, and of future, more powerful X-ray telescopes like Constellation-X and XEUS, Hellsten, Gnedin, & Miralda-Escudé (1998, hereafter HGM) and Perna & Loeb (1998) proposed the concept of an “X-ray forest,” a pattern of resonant metal absorption lines analogous to the Ly α forest. Using a hydrodynamic cosmological simulation,

HGM predicted distribution functions of O VII and O VIII absorption. Perna & Loeb (1998) and Fang & Canizares (2000) used analytic methods based on the Press-Schechter (1974) mass function to make similar predictions, considering additional ionic species and a range of cosmological models. X-ray afterglows of γ -ray bursts could also be used as background sources, in addition to bright quasars (Fiore et al. 2000).

This paper examines the X-ray forest phenomenon in a large, smoothed particle hydrodynamics (SPH) simulation of the Λ CDM model (inflationary cold dark matter with a cosmological constant). We extend the work of HGM by considering a wider range of ionic species, looking more closely at the physical state of the gas responsible for X-ray absorption, and examining the prospects for detection of the X-ray forest with current and next-generation X-ray telescopes. Our study is similar in approach to the recent work of Fang, Bryan, & Canizares (2002a, hereafter FBC), but there are significant differences in the atomic processes incorporated in the calculations (see §2.5) and differences in focus of the analysis.

The recent detection of a high density of O VI(1032Å, 1038Å) absorbers (Tripp & Savage 2000; Tripp, Savage, & Jenkins 2000; Savage et al. 2002) offers a tantalizing hint of a baryon component that might correspond to the warm-hot IGM. Although we have not designed our study primarily for O VI predictions, we do calculate the expected incidence of O VI absorption and investigate the connections between O VI absorbers and X-ray forest systems (O VII and O VIII). Cen et al. (2001) and Fang & Bryan (2001) provide detailed O VI predictions using hydrodynamic simulations.

The next section describes our SPH simulation and our methods for calculating X-ray forest absorption. Section 3 presents our predictions for the equivalent width distributions of a variety of metal lines and discusses the feasibility of detection. Section 4 focuses on the physical properties of the strong oxygen absorbers, which appear to be the most promising targets for the near future. We summarize our results in §5.

2. Modeling Methods

2.1. Cosmological simulation

The cosmological simulation analyzed here is identical to the simulation D1 described in Davé et al. (2001). Some illustrations of structure in this simulation appear in Figures 11 and 12, which are discussed in §4 below. We adopt a flat Λ CDM model with $\Omega_m = 0.4$, $\Omega_\Lambda = 0.6$, $h = 0.65$, $\Omega_b = 0.0473$, and the primordial power spectrum predicted by the inflationary CDM model with an inflationary spectral index $n = 0.95$ and normalization $\sigma_8 = 0.8$. This cosmological model is consistent with observational constraints from the cosmic microwave background, large scale structure, galaxy clusters, the Ly α forest, and Type Ia supernovae, though the value of Ω_m is somewhat higher than favored by the most recent measurements (Spergel et al. 2003). The simulation box is a periodic cube of side-length $50h^{-1}$ comoving Mpc. At the start of the simulation,

it contains 144^3 dark matter particles and an equal number of gas particles; some of the gas particles are converted to collisionless star particles during the course of the calculation. The masses of individual dark matter and gas particles are $6.3 \times 10^9 M_\odot$ and $8.5 \times 10^8 M_\odot$, respectively. The simulation is evolved from $z = 49$ to $z = 0$ using the parallel version (Davé, Dubinski, & Hernquist 1997) of TreeSPH (Hernquist & Katz 1989; Katz, Weinberg, & Hernquist 1996), which utilizes a tree algorithm for gravitational forces and SPH for hydrodynamic interactions. The gravitational force resolution is $7h^{-1}\text{kpc}$ (equivalent Plummer softening), in comoving units. The spatial resolution of the hydrodynamic calculation varies with density because of the Lagrangian nature of the SPH algorithm; all gas dynamical quantities are computed by smoothing with a symmetric spline kernel that encloses 32 SPH particles, or at most $2.7 \times 10^{10} M_\odot$ of baryons, with a minimum SPH smoothing length of $2.5h^{-1}\text{kpc}$ (comoving).

The simulation incorporates shock heating and Compton and radiative cooling, as well as adiabatic heating and cooling. Radiative cooling rates are computed for a primordial composition gas, as described by Katz, Weinberg, & Hernquist (1996). Cold gas in regions with density comparable to the Galactic interstellar medium is converted into stars; since this has little impact on the IGM at the densities and temperatures relevant to the X-ray forest, we refer the reader to Katz, Weinberg, & Hernquist (1996) for a discussion of the star formation algorithm. At the mass resolution of this simulation, inclusion of heating by a photoionizing background artificially suppresses the formation of galaxies (Weinberg, Hernquist, & Katz 1997a), so the simulation was run without a photoionizing background. As a consequence, expansion of the universe cools unshocked gas to very low temperatures (less than 100 K). In higher resolution simulations that incorporate a photoionizing background (Davé et al. 1999), unshocked gas at redshift $z = 0$ follows a tight temperature-density relation, $T \approx 10^4(\rho/\bar{\rho}_b)^{0.6}$ K, which arises from the competition between photoionization heating and adiabatic cooling (Hui & Gnedin 1997). (The mean temperature for this cosmological model is higher than that in the Davé et al. [1999] simulations because of the higher baryon density.) Before analyzing the simulation, therefore, we raise the temperatures of all gas particles with baryon overdensity $\delta_b < 100$ and $T < 10^4\delta_b^{0.6}$ K so that they lie on this temperature-density relation. We do not adjust the temperatures of shock-heated gas particles that already lie above this relation. This after-the-fact adjustment is a good approximation to the gas temperatures we would obtain in a simulation with an ionizing background. Most of the significant X-ray forest absorption will come from hotter, denser gas that is unaffected by this adjustment.

In this paper, we concentrate entirely on the $z = 0$ output of the simulation. Owing to the difficulty of detecting X-ray forest lines at all (as discussed in §3 below), observational studies are likely to focus on the quasars with the highest apparent X-ray fluxes, and hence on low redshift. We obtain density, temperature, and peculiar velocity profiles along 1200 randomly chosen lines of sight through the simulation cube, 400 in each projection, using the algorithm described by Hernquist et al. (1996), as implemented in Katz & Quinn’s code TIPSY.³ Each line of sight is divided into 5000

³<http://www-hpcc.astro.washington.edu/tools/tipsey/tipsey.html>

bins, so that each bin has a width of 1 km/s in velocity units, which is much finer than the few hundred km/s spectral resolution typical of the current and next generation X-ray telescopes. The contribution of each gas particle to each bin of the profile is calculated by a line integral through its spherically symmetric spline kernel, with contributions going to zero beyond the smoothing scale that encloses 32 SPH neighbors. We use the densities and temperatures to compute ionic species abundances as described below (§2.5), then calculate absorption spectra in redshift space by accounting for peculiar velocities and thermal broadening. We treat the projection axis of the cube as the redshift direction and make use of the periodic boundary, so a feature that would be “shifted out” of the cube by its peculiar velocity reappears at the opposite side. Except for the computation of ionic abundances, the calculation is entirely analogous to the calculation of Ly α forest absorption by Hernquist et al. (1996).

2.2. Selection of transition lines

Consider an absorption system of a given temperature, density, and path length. The strength of the absorption line produced by a given transition of a given ion is proportional to the path length, the transition oscillator strength, the abundance of the element in question, and the fraction of that element in the given ionization state, which depends in turn on the temperature, density, and the ionizing background radiation. The predicted number of lines per unit redshift also depends on the covering factor of absorbers with the temperature, density, and path length required to yield detectable absorption. To decide which lines to consider in our study, we first made a preliminary screening of all of the ions and transition lines listed in Verner, Verner, & Ferland (1996). We selected those with element abundance greater than 10^{-7} and resonance lines with energy above 0.25 keV ($\lambda < 50\text{\AA}$). For each ion we selected the resonance line with the greatest oscillator strength. We then calculated the total absorption produced along all 1200 lines of sight through the simulation box, i.e., the summed equivalent widths of all of the absorption lines produced by these transitions, and ranked the ions accordingly. The ions that produced at least one of the ten strongest lines are listed in Table 1. In addition to O VII and O VIII, we found that C V, C VI, N VI, N VII, Ne IX, Ne X, Si XIII, and Fe XVII produce relatively large amounts of absorption.

Detection of X-ray forest lines requires that the observed energy be larger than ~ 0.2 keV, both because of instrumental sensitivity and to avoid absorption by the Galactic interstellar medium. Lines in Table 1 with energy E can therefore be observed only to a maximum redshift $z = E/(0.2 \text{ keV}) - 1$. Fang & Canizares (2000) have used Press-Schechter models to predict absorption by O VIII and by two ionic species with much higher transition energies, Si XIV (2.01 keV) and Fe XXV (6.70 keV), which can potentially be observed out to high redshifts (see also Perna & Loeb 1998). These last two ionization states become abundant only at the high temperatures ($T \sim 10^7 \text{ K}$ and $T \sim 10^8 \text{ K}$, respectively) characteristic of rich galaxy clusters, which are poorly represented in our simulation box owing to its limited size. We therefore do not attempt to make predictions for these ions. The analytic method used by Fang & Canizares (2000) is well adapted

to the study of these highly ionized species, which are likely to occur only in the virialized regions that are best described by the Press-Schechter approximation and which are too rare to be well represented in our hydrodynamic simulation. Our numerical approach complements this analytic method by allowing more accurate investigation of lower ionization species, which may be found in lower density, unvirialized regions.

2.3. Metal abundance

The C IV and O VI absorption associated with Ly α forest lines implies that the metallicity of the low density IGM is $\sim 10^{-3} - 10^{-2}$ of solar at high redshift (see, e.g., Songaila & Cowie 1996; Haehnelt, Steinmetz, & Rauch 1996; Hellsten et al. 1997; Davé et al. 1998; Ellison et al. 2000; Schaye et al. 2000). At low redshift ($z \simeq 0.5$), Barlow & Tytler (1998) found $[\text{C}/\text{H}] \simeq -1.6$ for HI absorbers with $W_r \sim 0.5\text{\AA}$ using Hubble FOS data. In the denser IGM of X-ray clusters, on the other hand, the inferred metal abundance is as high as one third of solar (Mushotzky et al. 1996). Unfortunately, these observations give little guidance to the metallicity of the regions with $\delta \sim 10 - 1000$ that are responsible for the X-ray forest at $z = 0$. While metal enrichment can be tracked in a simulation either during dynamical evolution, as in HGM and Cen et al. (2001), or in post-processing, as in Aguirre et al. (2001), the numerical predictions are sensitive to the uncertain details of metal ejection from the immediate vicinity of galaxies. Rather than adopt an explicit but model-dependent prescription for the metallicity as a function of environment, we will generally assume that the metallicity of the medium that produces X-ray forest absorption is $0.1Z_\odot$, intermediate between the Ly α forest and cluster IGM values. We also assume that the relative abundances of the different elements are similar to those in the Sun; some authors (e.g., FBC) have adopted enhanced abundances of α -elements (oxygen in particular), characteristic of Type II SN enrichment. Since most absorbers are unsaturated, predicted equivalent widths are simply proportional to the assumed metallicity, but this proportionality breaks down for the strongest absorbers. We discuss the impact of different metallicity assumptions, in particular the effects of including a density-dependent metallicity and scatter about the mean metallicity-density relation (Cen & Ostriker 1999b), in §3.1 below.

2.4. The X-ray background

As discussed below in §2.5, ionic abundances are affected by both collisional ionization and photoionization. To compute the latter, we must adopt an intensity and spectrum of the X-ray background, which contains the ionizing photons that are relevant to these high ionization species. For most of our calculations, we adopt the background of Miyaji et al. (1998, hereafter Mi98), which was based on ASCA and ROSAT data:

$$J_x(E) = J_1 \left(\frac{E}{\text{keV}} \right)^{-0.42}, \quad (1)$$

where $J_1 = 6.626 \times 10^{-26} \text{ erg cm}^{-2}\text{s}^{-1}\text{sr}^{-1}\text{Hz}^{-1}$. This has a higher intensity and slightly steeper slope than the Barcons & Fabian (1992, hereafter BF92) background, which was adopted by HGM. The BF92 background spectrum is

$$J_x(E) = J_0 \left(\frac{E}{E_X} \right)^{-0.29} e^{-E/E_X}, \quad (2)$$

where $E_X = 40 \text{ keV}$ and $J_0 = 1.75 \times 10^{-26} \text{ erg cm}^{-2}\text{s}^{-1}\text{sr}^{-1}\text{Hz}^{-1}$. Figure 1 plots the BF92 and Mi98 background spectra as dotted and short-dashed lines, respectively.

Extrapolation of these X-ray background fits to longer wavelengths substantially underestimates the flux expected from quasars and star-forming galaxies. While the UV photoionizing background makes little difference for high ionization X-ray lines, it does matter for determining the ionic abundances of HI, O VI, and, at relatively low densities and temperatures, O VII. We therefore include a UV background

$$J_{\text{UV}}(E) = J_2 \left(\frac{E}{1 \text{ Ryd}} \right)^{-1.8}, \quad (3)$$

with $J_2 = 2.4 \times 10^{-23} \text{ erg cm}^{-2}\text{s}^{-1}\text{sr}^{-1}\text{Hz}^{-1}$, based on Shull et al. (1999). This background is shown by the long-dashed line in Figure 1. We generally use the Mi98 spectrum at energies $E \geq 0.25 \text{ keV}$ and the UV background (3) at energies $E < 0.25 \text{ keV}$, where it exceeds the Mi98 spectrum, though we have repeated some of our calculations for different background choices as discussed below.

2.5. Ionization fractions

We calculate the ionization fraction for each ion at a number of temperature and density grid points with an assumed radiation background, using the publicly available code Cloudy (Ferland 1996). The ionization fraction of each ion for any given temperature and density is then obtained by interpolation.

Figures 2 and 3 illustrate the resulting ionization fractions that enter our calculations. Figure 2 show results for the hydrogen-like, helium-like, and lithium-like states of oxygen (top row), nitrogen (middle row), and carbon (bottom row). Curves in the central panels are calculated using our standard radiation background for a gas density $n_H = 10^{-5} \text{ cm}^{-3}$, which corresponds to a baryon overdensity $\delta_b = 60$ at $z = 0$ for our adopted cosmological parameters. Right-hand panels show calculations for $n_H = 10^{-6} \text{ cm}^{-3}$, an overdensity $\delta_b = 6$. Left-hand panels show results for collisional ionization only, in which case ionization fractions are independent of density. (We actually compute these curves using $n_H = 10^{-5} \text{ cm}^{-3}$ and a radiation background reduced in intensity by a factor of 10^4 .)

Since oxygen, nitrogen, and carbon all exhibit similar behavior, we restrict ourselves to oxygen in the following discussion. In the absence of photoionization, the fragile, lithium-like species O VI

exists only over a narrow temperature range, $T \sim 2 - 5 \times 10^5$ K, and even in this range its fractional abundance never exceeds 0.25. The helium-like state, O VII, dominates a much wider temperature range, with a fraction exceeding 0.5 for $T \sim 0.3 - 2.1 \times 10^6$ K. At higher temperatures, O VII begins to give way to O VIII, though the O VIII fraction never exceeds ~ 0.3 because temperatures high enough to produce O VIII are also high enough to produce O IX (not shown on the plot). Similarly, at low temperatures O VII and O VI give way to lower ionization species.

At these densities, photoionization has a major impact on the predicted abundances. There is still a general trend of moving from O VI to O VII to O VIII as the temperature increases, but with photoionization included each species occupies a much wider temperature range, and there are more temperatures at which multiple species co-exist. For $\delta_b = 6$, the peak O VIII fraction occurs at $T \sim 2 \times 10^5$ K, and the O VII fraction peaks at $T \sim 10^4$ K. For $\delta_b = 60$, the recombination rates are higher relative to the photoionization rates, so the curves shift towards those of pure collisional ionization, but even in this case O VII remains significant down to temperatures of several $\times 10^4$ K and O VIII to several $\times 10^5$ K. More generally, for the densities characteristic of intergalactic filaments or the outskirts of clusters and groups, photoionization allows a species to exist at temperatures far below those deduced from the collisional equilibrium ionization fractions.

The behavior of nitrogen and carbon is entirely analogous to that of oxygen, except that all the curves are shifted towards lower temperature owing to the lower ionization energies. For the more highly ionized species shown in Figure 3, photoionization is usually much less significant, since there are fewer high energy photons. However, it still makes a difference in some cases for $\delta_b = 6$. Note the expanded temperature scale of Figure 3 relative to Figure 2. The highly ionized iron species, Fe XXV and Fe XXVI, occur only at the high temperatures characteristic of rich clusters, though Fe XVII occurs at the lower temperatures characteristic of the WHIM.

Figure 4 shows the dependence of the oxygen predictions on the adopted radiation background. In each panel, heavy and light lines show the ionization fractions for the Mi98 and BF92 X-ray background spectra, respectively. Upper panels show results including the UV background spectrum of equation (3) (using the maximum of the X-ray background and UV background at each wavelength), and lower panels show results using the X-ray background only. There is little difference between the results that use the Mi98 or BF92 spectra, indicating that uncertainties in the X-ray background should introduce little uncertainty in our predictions. However, the UV background makes a significant difference for O VI and to some extent O VII, particularly at higher densities and lower temperatures. Uncertainty in the intensity and spectral shape of the UV background introduces some uncertainty in our O VI predictions, but it should make little difference to our predictions of X-ray absorption.

It is worth noting at this point the two main physical differences between our calculations and those of FBC. The first is that our simulation incorporates radiative cooling, which changes the temperature structure of collapsed regions and allows some of the gas to condense into galaxies, removing it from the IGM. The second is that our analysis incorporates photoionization, while

FBC only include collisional ionization. As we can see from Figures 2-4, photoionization makes an important difference for oxygen, nitrogen, and carbon, though it is less significant for higher ionization species. FBC also assume a much higher metallicity, with an oxygen abundance of 0.5 solar, but this difference just shifts absorber column densities by a factor of five. Our input physics is similar to that of HGM, who incorporate radiative cooling and photoionization using the BF92 X-ray background but do not include a UV background.

2.6. Calculating absorption

The transmitted X-ray flux is

$$F(\nu_0) = F_c(\nu_0) \left(1 - e^{-\tau(\nu_0)}\right), \quad (4)$$

where F_c is the quasar's X-ray continuum multiplied by the instrument response function and $\tau(\nu_0)$ is the optical depth at observed frequency ν_0 . We will assume that the continuum can be determined and divided out, so we define $F_c(\nu_0) \equiv 1$ in equation (4) and refer to the transmitted flux $F(\nu_0) = (1 - e^{-\tau(\nu_0)})$ as the simulated spectrum. Strong atomic features are rare in this wavelength regime, so continuum estimation is relatively straightforward if the signal-to-noise ratio of the spectrum is high enough.

The absorption spectrum is determined by a convolution of the ion number density along the line of sight with the absorption line profile,

$$\tau(\nu_0) = \sum_{Z,I,l} \int dx \frac{\pi e^2}{m_e c} f_l \phi(x, \nu_0) n_{Z,I}(x), \quad (5)$$

where Z, I, l label the atomic number, the ionization stage, and the transition line of the ion, respectively, f_l is the oscillator strength of the transition, and $n_{Z,I}(x)$ is the ion number density. If we assume that the relative abundances of heavy elements are similar to those of the Sun, we can write

$$n_{Z,I}(x) = n_H(x) Y_{Z\odot} \mathcal{F}_{Z,I}(x) \left(\frac{Z}{Z_\odot}\right), \quad (6)$$

where $\mathcal{F}_{Z,I}(x)$ is the ionization fraction for the (Z, I) ion computed from the density and temperature at position x , $n_H(x)$ is the number density of hydrogen atoms, $Y_{Z\odot}$ is the solar abundance of element Z by number relative to hydrogen, and Z/Z_\odot is the metallicity relative to solar. (We regret the use of Z for two different purposes in the same equation but see no better alternative). The line profile $\phi(x, \nu_0)$ is

$$\phi(x, \nu_0) = \varphi \left[T(x), \left(1 + z(x) + \frac{u(x)}{c}\right) \nu_0 \right], \quad (7)$$

where $z(x)$ is the Hubble redshift at x , $u(x)$ is the peculiar velocity, and

$$\varphi_l[T, \nu] = \frac{e^{-(\nu - \nu_l)^2 / \Delta \nu_D^2}}{\sqrt{\pi} \Delta \nu_D} \quad (8)$$

is the thermal broadening profile with Doppler linewidth $\Delta\nu_D = \nu_l \sqrt{2kT/mc^2}$, where m is the ion mass. We do not incorporate damping wings in the line profile, but they are negligible for these weak absorption lines.

As described in §2.1, the average density, temperature, and velocity of gas for each of the 5000 bins in a line of sight were extracted from the simulation using TIPSY. For each ion of interest, we calculate the ionization fraction for these temperature and density values by interpolating among the Cloudy outputs. The optical depth along each line of sight is then obtained by carrying out the convolution, equation (5), numerically. We consider each ionic species in isolation, so in practice we do not perform the sum in equation (5), only the integral. Because X-ray forest lines are rare and the bright quasars amenable to study with present instruments are at low redshifts, there will usually not be much ambiguity in identification of features.

2.7. Absorbers

Figure 5 shows a sample O VII absorption spectrum, one that contains a strong feature. As the lower panels demonstrate, this absorption feature arises in the hot gas halo of a moderate sized group, with a typical gas temperature of a few $\times 10^6$ K. For clarity, we have ignored peculiar velocities when calculating these profiles, but we include thermal broadening in the optical depth and flux profiles. The dashed line in the top panel shows the redshift-space spectrum, in which the absorption feature is shifted by peculiar velocity but not changed substantially in width or depth. In all of our statistical calculations below, we identify absorbers and measure their properties from the redshift-space spectrum, including peculiar velocities.

We identify absorbers using a simple threshold algorithm: an absorber is defined as a region where all the pixels have absorption above a given threshold. Because X-ray forest absorbers are likely to be unresolved or nearly unresolved, at least for the foreseeable future, more elaborate algorithms that deblend distinct peaks or fit superpositions of Voigt profiles are unnecessary for our present purposes. We adopt an absorption threshold of 0.01, hence absorbers consist of contiguous pixels with transmitted flux less than 0.99. We have checked the effect of using different thresholds and found that while the number of weak absorbers is slightly suppressed by a higher threshold, the number of strong absorbers is insensitive to the threshold value. In Figure 5, the boundary of the absorber is marked by ticks on the spectrum.

The equivalent width of an absorber is

$$W = \int_{v_{\min}}^{v_{\max}} dv \left(1 - e^{-\tau(v)} \right), \quad (9)$$

where $v = cz + u$, and τ is the optical depth. The equivalent width defined in this way has velocity units. Conversions to other useful units are $W = 6.67(W/100 \text{ km s}^{-1})(\lambda/20 \text{ \AA}) \text{ m\AA} = 0.33(W/100 \text{ km s}^{-1})(E/1 \text{ keV}) \text{ eV}$, where λ and E are the observed line wavelength and energy, respectively. For optically thin absorbers, there is a linear relation between equivalent width and

column density,

$$W_{\text{thin}} = \frac{\pi e^2}{m_e c} \lambda f_{Z,I} N_{Z,I} , \quad (10)$$

where $N_{Z,I}$ is the column density and $f_{Z,I}$ is the transition oscillator strength. Since X-ray forest lines are weak and fairly broad, equation (10) is usually a good approximation. However, the equivalent widths of the strongest absorbers are depressed by saturation. Figure 6 demonstrates this effect, plotting the ratio of actual equivalent width to the optically thin value of equation (10) for the O VII and O VIII absorbers along our 1200 lines of sight. The upper panels show results using our standard metallicity $Z = 0.1Z_\odot$, and the lower panels show results using $Z = Z_\odot$, i.e., a factor of ten increase in absorber column densities. For O VII, saturation becomes significant above $N \sim 2 \times 10^{15} \text{ cm}^{-2}$, $W \sim 80 \text{ km s}^{-1}$, and by $N \sim 4 \times 10^{15} \text{ cm}^{-2}$ the equivalent width is typically depressed by a factor of two. There are very few absorbers in this regime for $Z = 0.1Z_\odot$, but a significant number for $Z = Z_\odot$. Saturation of O VIII lines does not become significant until $N \sim 10^{16} \text{ cm}^{-2}$, and we find few absorbers of this column density even with $Z = Z_\odot$. We will generally present our results in terms of equivalent width (including saturation effects) because this quantity is more directly determined from observations, but we also label our plots by the corresponding optically thin column density of equation (10), to aid with physical interpretations and to compare with other numerical and analytic predictions.

3. Equivalent Width Distributions and the Detectability of the X-ray Forest

3.1. Equivalent width distributions

Figure 7 presents our principal quantitative prediction, the cumulative distribution of O VII and O VIII absorbers as a function of equivalent width. We plot $dN/d\ln(1+z)$, which is equivalent to the number of lines per unit redshift at $z = 0$. Adopting the BF92 background in place of the Mi98 one, or omitting the additional UV background at longer wavelengths, makes a nearly imperceptible difference to these curves. As mentioned earlier, the number of weak absorbers would be lower if we adopted a higher threshold for the line identification algorithm, but the number of strong absorbers would be unaffected. We also find that the peculiar velocities have little effect on the equivalent width distribution, though they change the equivalent widths of individual absorbers to some extent. The solid lines in each panel show our standard case of uniform metallicity with $Z = 0.1Z_\odot$. The shapes of the O VII and O VIII distributions are similar, with somewhat fewer high equivalent width lines for O VIII. The number of O VII lines drops to one per unit redshift at $W \sim 40 \text{ km s}^{-1}$ (25 km s^{-1} for O VIII) and falls rapidly for larger W . The paucity of stronger absorbers is not surprising: for $Z = 0.1Z_\odot$, a 1 Mpc path length through a medium with $n_H = 10^{-5} \text{ cm}^{-3}$ ($\delta_b = 60$) and an O VII fraction of 0.5 yields a column density of $1.1 \times 10^{15} \text{ cm}^{-2}$, or $W \sim 40 \text{ km s}^{-1}$, and longer path lengths at such high density and O VII fraction are rare.

Dotted curves in Figure 7 show predictions for a solar metallicity IGM. The increase in oxygen abundance boosts the column density of each absorber by the same factor, and at low W the

equivalent width distribution simply shifts to the right by a factor of ten. At high W the rightward shift is smaller, since saturation begins to suppress the linear relation between equivalent width and column density; the high- W tails of the solar metallicity distribution functions are therefore steeper. Because the equivalent width distribution falls steeply at high W even for $Z = 0.1Z_{\odot}$, a modest increase in metallicity can still translate into a large increase in the predicted number of systems above some threshold — i.e., a small horizontal shift creates a large vertical shift. Labeled vertical error bars in Figure 7 show representative 5σ detection thresholds for several different X-ray satellites, which we discuss in §3.2 below. Unfortunately, one can already see that a comprehensive study of the X-ray forest with current instruments will be challenging unless the IGM has near solar metallicity, which seems unreasonably optimistic. The remaining curves in Figure 7 are discussed at the end of the Section, where we consider the potential impact of non-uniform metallicity.

The equivalent width distributions for the other ions listed in Table 1 are shown in Figures 8 and 9, computed assuming 0.1 solar metallicity and the Mi98+UV background. The number of high equivalent width absorbers is generally much smaller than for O VII or O VIII. Roughly speaking, one can think of the lower element abundances and, in some cases, weaker transition oscillator strengths as shifting the previous equivalent width distributions towards lower W , though of course the distribution also depends on the occurrence of density and temperature regimes where these ions have a high fractional abundance. As a guide to relative observability, we list in Table 1 the equivalent width threshold above which we find one absorber per unit redshift in our simulated spectra for our standard assumptions. This threshold is roughly proportional to the adopted metallicity, though it would increase more slowly above $W \sim 100 \text{ km s}^{-1}$ because of saturation (see Figure 6). C V and C VI have the strongest absorption after oxygen, but their strong resonance lines lie at 40.3\AA and 33.7\AA , respectively, which restricts their observability to relatively low redshift quasars and puts them in a range of poorer instrument sensitivity even at zero redshift. Fe XVII and Ne IX produce the next strongest absorption; their transition energies are higher, but the predicted equivalent widths are a factor ~ 2 lower than those of C V and C VI.

While the focus of this paper is X-ray absorption, the $(1032\text{\AA}, 1038\text{\AA})$ UV doublet of O VI is another potential tracer of intergalactic gas at these densities and temperatures, and is observable from Hubble Space Telescope or the Far Ultraviolet Spectroscopic Explorer (FUSE). Recent observations have detected a number of O VI absorbers towards low redshift quasars, implying a high number density $dN/dz \sim 20 - 50$ of lines with rest-frame equivalent width $W_r > 30\text{m\AA}$ (Oegerle et al. 2000; Tripp, Savage, & Jenkins 2000; Tripp & Savage 2000; Tripp et al. 2001; Savage et al. 2002). Figure 10 shows the cumulative equivalent width distribution of the 1032\AA line of O VI absorbers predicted by our simulation, together with data points from Tripp, Savage, & Jenkins (2000) and Savage et al. (2002) (taken from figure 2 of Cen et al. 2001). We have used the Mi98+UV background, but the results are not very sensitive to this choice. As in Figure 7, solid and dotted curves show predictions for uniform metallicity $Z = 0.1Z_{\odot}$ and $Z = Z_{\odot}$, respectively; long-dashed and dot-short dashed curves show predictions that incorporate non-uniform metallicity with typical $Z \sim 0.1Z_{\odot}$, as discussed at the end of the Section. For any of the metallicity models except

$Z = Z_{\odot}$, the simulation results are in good agreement with the observations, though we caution that our threshold algorithm may not be as good a match to the analyses of these higher resolution, UV data. The dot-long dashed curve of Figure 10 shows the results of Fang & Bryan (2001), who carried out similar calculations using a different numerical method, with a metallicity model similar to that shown by our dot-short dashed line. The agreement between the two calculations is remarkably good. These results also agree fairly well with those of Cen et al. (2001), though Cen et al. predict somewhat less absorption than observed. Simultaneous detections of O VI, O VII, and O VIII could provide insight into the physical state of the absorbing medium; we discuss the expected correlations between these ionization phases in §4 below.

In principle, O VI absorption can also be studied with X-ray telescopes, using the KLL resonance of the photoionization cross-section, i.e., excitation-autoionization via the $1s \rightarrow 2p$ transition resulting in $1s2s2p$ (KLL) resonance.⁴ The strongest transition has $\lambda = 22.05 \text{ \AA}$, $f = 0.408$ (Pradhan 2000). The dashed line at the lower left of Figure 10 shows the equivalent width distribution for this absorption. It is weaker than the corresponding O VII and O VIII absorption (compare to Figure 7), primarily because of the lower fractional abundance of O VI. X-ray detection of intergalactic O VI absorption is therefore unlikely, at least without a substantial increase in instrumental sensitivity.

The closest point of comparison for our calculation is that of HGM, who used a different numerical method but similar input physics. They present their O VII and O VIII predictions in the form of differential distributions, whereas we have shown cumulative distributions in Figure 7, but we have also created differential plots (not shown) and compared results. At small equivalent width, we have excellent agreement with HGM. However, the number of strong absorbers in our simulation (for our standard metallicity assumption $Z = 0.1Z_{\odot}$) falls short of the number in theirs by a factor of a few — or, equivalently, for absorbers that have a frequency ~ 1 per unit redshift, we predict a lower equivalent width by a factor $\sim 2 - 4$. The cosmological parameters adopted by HGM are slightly different from ours, in the direction of increasing the number of absorbers (they have $\sigma_8 = 0.97$, $h = 0.7$, $\Omega_b = 0.05$). Our box size of $50h^{-1}\text{Mpc}$ is intermediate between those of the two simulations used by HGM, $64h^{-1}\text{Mpc}$ and $32h^{-1}\text{Mpc}$, but close enough to their larger box that this difference seems unlikely to have a large systematic effect. The total number of absorbers in the simulations at the equivalent widths where we disagree is small, and it could be that the difference simply reflects statistical fluctuations in the structure present in the two simulation volumes. However, we think that the most likely source of difference is the treatment of IGM metallicity: we assume a uniform metallicity of 0.1 solar, whereas HGM track the spread of metals in their simulation, so that the metallicity varies with spatial position. They comment that typical metallicities are $\sim 0.1Z_{\odot}$ in the density and temperature range that dominate X-ray forest absorption, but they do not plot the scatter in metallicity, and it could be that the strongest absorption occurs in regions where the metallicity is higher than average. Cen & Ostriker (1999b)

⁴This interesting possibility was pointed out to us by Jordi Miralda-Escudé and Anil Pradhan.

find a substantial scatter in metallicity at fixed overdensity in their hydrodynamic simulations, with a mean of $0.1Z_{\odot}$ at $\delta \approx 20$ and 1σ variations of a factor of 2–3. This effect would rather naturally explain the difference between our results and HGM’s, with agreement at low W but disagreement in the steeply falling tail of the distribution.

To address this point quantitatively, we show two additional curves in each panel of Figure 7, calculated for a non-uniform metallicity with statistical properties based on figure 2 of Cen & Ostriker (1999b). Dashed curves show the impact of metallicity scatter alone. We compute them by drawing the metallicity of each line of sight independently from a log-normal distribution with $\langle \log Z/Z_{\odot} \rangle = -1$ and $\sigma_{\log Z} = 0.4$. Because we assign a single metallicity to a given line of sight, the fluctuation above or below the mean is coherent across each absorber. At low equivalent widths, where the distribution functions are shallow, metallicity scatter has little impact. For rare systems, however, the value of W at a given value of $dN/d\ln(1+z)$ increases by a factor of 2–3, since there are more intrinsically low column density systems to scatter to high metallicity than vice versa. Dot-dashed curves show the effect of incorporating a density-dependent mean metallicity, with $\langle \log Z/Z_{\odot} \rangle = -1.66 + 0.36 \log \delta$, while retaining log-normal scatter about the mean metallicity as before. This change depresses the distribution function at lower W , where systems typically arise in lower density gas. We conclude that the differences in metallicity treatment could plausibly account for most of the difference between our calculations and that of HGM, and that a metallicity distribution similar to that of Cen & Ostriker (1999b) would increase the predicted equivalent widths of rare systems (at fixed line density) by a factor ~ 2 relative to our uniform, $Z = 0.1Z_{\odot}$ case. We also show O VI predictions for these non-uniform metallicity models in Figure 10; the qualitative effect of non-uniform metallicity is similar, but the quantitative impact at the equivalent width thresholds of the observational data points is modest because these points do not lie on the extreme tail of the distribution.

FBC predict a much higher occurrence of strong O VII and O VIII absorption than either HGM or our standard model, but this difference is mainly attributable to their higher assumed oxygen abundance of $0.5Z_{\odot}$, also adopted in the analytic calculations of FC and Perna & Loeb (1998). (These papers also use an older solar abundance for oxygen that is slightly higher than the one adopted here. In our units, their abundance would be $0.576Z_{\odot}$.) Direct comparison of our Figure 7 to FBC’s figure 13 is difficult because they show differential distributions of column density while we show cumulative distributions of equivalent width (including saturation effects). However, T. Fang has kindly provided the FBC O VII data in numerical form, and we have made direct comparisons of the column density distributions. At high column densities ($N \gtrsim 5 \times 10^{15} \text{ cm}^{-2}$), the FBC results for oxygen abundance $0.576Z_{\odot}$ lie very close to our results for $Z = Z_{\odot}$. (Recall that in this regime, the equivalent widths in Figure 7 have typically been depressed by a factor of two or more relative to their optically thin values.) The fact that the predictions match for metallicities that differ by a factor of 1.7 can plausibly be attributed to the presence in our simulation of radiative cooling, which converts some of the hot gas in collapsed halos into cold gas and stars. At lower column densities, our solar metallicity model predicts substantially more absorbers than FBC (e.g.,

by a factor ~ 7 at $N \sim 10^{14} \text{ cm}^{-2}$). The difference in the shapes of the distribution functions can be plausibly attributed to the impact of photoionization, which becomes important at the lower densities and temperatures characteristic of weaker O VII systems.

Once we allow for differences in assumptions about metallicity, we find the general level of agreement between our results and those of HGM and FBC (and Cen et al. 2001 and Fang & Bryan 2001 for O VI) to be encouraging. It suggests that, at the factor of two level, the X-ray forest predictions from hydrodynamic simulations are not sensitive to the numerical methodology, or even to the inclusion of radiative cooling and star formation, and that photoionization is significant for weaker absorption systems but not for the strongest absorbers. The largest uncertainty in the predictions is the poorly known metallicity distribution of the IGM, and for O VI, the strength of the metagalactic flux at ~ 9 Ryd. FBC compare their numerical results to the analytic, Press-Schechter based approach of FC and Perna & Loeb (1998) in some detail. They find that the analytic approach works well for high-excitation ions (e.g., Fe XXV and Fe XXVI) and for the highest column density systems of lower excitation ions (e.g., $N \gtrsim 10^{16} \text{ cm}^{-2}$ for O VII and O VIII), while it tends to underestimate the occurrence of weaker absorption, which often arises outside of the collapsed halos modeled by the Press-Schechter formalism.

3.2. Observational capabilities

The best spectral resolution of the current and next generation X-ray telescopes is $R \equiv \lambda/\Delta\lambda \sim 1000$, or about 300 km s^{-1} in velocity units. Most absorbers, therefore, are likely to be unresolved. In a quasar spectrum, the minimum detectable equivalent width for an unresolved absorption feature is

$$W_{\min} = \left(\frac{S}{N} \right)_{\min} \left(\frac{E}{RAF_x t} \right)^{1/2}, \quad (11)$$

where $(\frac{S}{N})_{\min}$ is the minimum signal-to-noise ratio required for detection, E is the observed energy of the line, t is the integration time, R is the spectral resolution, A is the effective area, and F_x is the photon flux, e.g., in units of photons $\text{cm}^{-2}\text{s}^{-1}\text{keV}^{-1}$. Equation (11) yields an equivalent width in the same energy units used for E and F_x . An X-ray spectrum of a moderate redshift quasar might have $N_{\text{res}} \sim 500$ resolution elements in which absorption could potentially fall, so the S/N threshold for a “blind” detection must be fairly high to avoid the spurious identification of noise peaks as absorption systems. We therefore adopt $S/N = 5$ as a threshold for secure detection in our discussion below. A 4σ feature would have a probability $\sim 3 \times 10^{-5} N_{\text{res}}$ of arising by chance, assuming Gaussian statistics, so it would be sufficient for a tentative detection.

The characteristics of each X-ray telescope depend on the choice of instrument setting (grating, detector, etc.). We will not discuss these issues in detail here, but we list in Table 2 some represen-

tative value of effective area and resolving power for *Chandra*⁵, *XMM-Newton*⁶, *Constellation-X*⁷ and *XEUS*.⁸ To assess detectability thresholds, we assume a quasar flux

$$F_x = F_0 \left(\frac{E}{E_0} \right)^{-\Gamma}, \quad (12)$$

and we adopt as an example the X-ray bright quasar H1821+643 ($z = 0.297$), with $F_0 = 2 \times 10^{-3}$ photons $\text{cm}^{-2}\text{s}^{-1}\text{keV}^{-1}$ at $E_0 = 1\text{keV}$, and $\Gamma = 2.35$ (S. Mathur, private communication; see Mathur, Weinberg, & Chen 2003 for more detailed discussion of H1821+643). We have not accounted for the effects of Galactic HI absorption, which depresses the flux by $\sim 30\%$ at wavelengths relevant to O VII or O VIII detection. Values of W_{\min} for $S/N = 5$ and an integration time of 500 ksec are listed in Table 3, for a variety of observed wavelengths.

Figures 7–9 show that for a given path length it is easiest to detect O VII and O VIII absorbers. However, as shown in Table 3, even a 500 ksec integration with the brightness of H1821+643 yields a minimum detectable equivalent width of $\sim 270 \text{ km s}^{-1}$ for *Chandra* and $\sim 160 \text{ km s}^{-1}$ for *XMM-Newton*. These limits are marked by vertical bars in Figure 7. Assuming a metallicity of 0.1 solar, the strongest absorbers in our simulated spectra have $W \sim 200 \text{ km s}^{-1}$, which are at best marginally detectable by *Chandra* and *XMM-Newton*. The curves with metallicity scatter are arguably more realistic than the constant metallicity case, for the reasons discussed by Cen & Ostriker (1999b), and it is possible that enriched regions of the IGM have enhanced ratios of α -elements like oxygen relative to iron. Both of these changes would improve the prospects of detection.

A search for O VII and O VIII absorption associated with known O VI absorption (from UV observations) holds considerably more promise than a blind search for X-ray forest absorption, for two reasons. First, when searching at a redshift that is known a priori, the required S/N for a significant detection is lower, $\sim 2 - 3\sigma$ instead of $\sim 5\sigma$, and at these equivalent widths the number of systems rises sharply with decreasing detection threshold. Second, as we will show shortly, the strongest O VI absorbers frequently have strong associated O VII absorption, though this is less true for O VIII.

Constellation-X, which is likely to be the next major advance in capability for X-ray spectroscopy, is now under design. For the observing conditions assumed in Table 2, the minimum detectable width for *Constellation-X* is about 25 km/s; thus, for a metallicity of 0.1 solar, we predict that *Constellation-X* could detect 2-3 O VII absorbers and ~ 1 O VIII absorber per unit redshift along each random line of sight, at 5σ significance. The numbers rise slightly if one adopts the Cen & Ostriker (1999b) metallicity-density relation, and if the metallicity is as high as solar

⁵<http://chandra.harvard.edu>

⁶<http://xmm.vilspa.esa.es>

⁷<http://constellation.gsfc.nasa.gov>

⁸<http://astro.estec.esa.nl/SA-general/Projects/XEUS>

then tens of absorber should be detected per line of sight. The powerful *XEUS* X-ray telescope, with a typical equivalent width threshold of $\sim 10 \text{ km s}^{-1}$, should be able to find large numbers of absorbers.

4. Physical Properties and Correlations of Oxygen Absorbers

We now turn to the physical state of the gas producing oxygen absorption, which appears to be the element most amenable to observational study. Figures 11 and 12 are a useful starting point. Figure 11 shows the gas particles in the simulation color-coded by temperature (upper left), density (upper right), O VII ion fraction (lower left), and O VIII ion fraction (lower right). We have zoomed in on a $(25h^{-1}\text{Mpc})^3$ sub-volume of the simulation in order to show finer details of the structure. Gas in virialized halos has been shock-heated to typical temperatures of $\sim 10^6 - 10^7 \text{ K}$, while gas in the filaments connecting these halos is typically somewhat cooler, from $\sim 10^5 \text{ K}$ to a few $\times 10^6 \text{ K}$. The regions of high O VII and O VIII ionization fractions trace the general structure of these filaments and halos. The O VII fraction shows fairly sharp peaks in the dense inner regions of the halos, though there is by no means a one-to-one correspondence between density peaks and peaks of O VII fraction. O VIII tends to dominate in the outer regions of halos and filaments, where the density is lower. The relatively massive, hot group at the center of the upper panels has low O VII and O VIII fractions because its temperature is high enough to fully ionize the oxygen to O IX.

Figure 12 shows the projected column density of O VII in the full $50h^{-1}\text{Mpc}$ simulation cube, with threshold column densities in the four panels of 10^{14} , $10^{14.5}$, 10^{15} , and $10^{15.5} \text{ cm}^{-2}$. The assumed IGM metallicity is 0.1 solar. At the 10^{14} cm^{-2} threshold, O VII traces a rich network of shock-heated filaments. At $10^{14.5} \text{ cm}^{-2}$, the stronger filaments remain, but the weaker ones disappear from view. By 10^{15} cm^{-2} , the distribution consists mainly of distinct clumps, occasionally connected by a more diffuse medium. At $10^{15.5} \text{ cm}^{-2}$, only the dense regions in collapsed halos are visible. The redshift path length through the simulation volume is only $\Delta z = 0.0167$, so the covering factor for absorption to a quasar of redshift z would be larger by $z/\Delta z$, e.g., by a factor of 18 for $z = 0.3$. The column density thresholds in the last three panels correspond roughly to the detectability thresholds for *XEUS*, *Constellation-X*, and *Chandra/XMM-Newton*, given the assumptions discussed in §3.2. If the IGM metallicity is $Z \sim 0.1Z_\odot$, therefore, current generation X-ray telescopes have the potential to detect X-ray forest absorption in high-density gas, *Constellation-X* can begin to reach into intergalactic filaments, and *XEUS* can map the filamentary structure. If the IGM metallicity is 0.3 solar, then the same panels represent column density thresholds that are ~ 0.5 dex higher, so the *Chandra/XMM-Newton* threshold would correspond to the lower left panel, the *Constellation-X* threshold to the upper right, and the *XEUS* threshold to the complex network of filaments in the upper left.

To quantify the physical properties of the oxygen absorption systems, we calculate the average temperature and overdensity of the gas associated with each absorber. We first define a *pixel*

temperature and density, assigning to each pixel along the line of sight a temperature and density that is an average of the gas density and temperature contributing to that pixel weighted by optical depth,

$$n_{\text{pix}}(v) = [\tau(v)]^{-1} \int dx \left(\frac{d\tau}{dx} \right) n(x), \quad (13)$$

$$T_{\text{pix}}(v) = [\tau(v)]^{-1} \int dx \left(\frac{d\tau}{dx} \right) T(x). \quad (14)$$

The absorber temperature and overdensity are then obtained by averaging (with equal weight) over the pixels belonging to that absorber. Thermal broadening allows gas of different densities and temperatures to contribute to a given pixel, but the optical depth weighting ensures that the average is not dominated by gas that is not actually responsible for the corresponding absorption.

Figure 13 plots the temperature and overdensity of each absorber against its equivalent width, for absorbers with $W \geq 10 \text{ km s}^{-1}$. The assumed metallicity is $Z = 0.1 Z_{\odot}$; for a higher assumed metallicity one would, in the optically thin approximation, simply shift each point horizontally by the same factor by which the metallicity is increased. Most O VI absorbers have temperature $10^{4.2} \text{ K} < T < 10^{5.7} \text{ K}$, O VII absorbers have $10^{4.5} \text{ K} < T < 10^{6.5} \text{ K}$, and O VIII absorbers $10^{5.2} \text{ K} < T < 10^{6.7} \text{ K}$. For all three species, there is a correlation between equivalent width and gas overdensity, though there are some notable outliers from these correlations. In the case of O VII absorbers, the median overdensity increases from $\delta \sim 10$ at $W \sim 10 \text{ km s}^{-1}$ to $\delta \sim 100$ at $W \sim 50 \text{ km s}^{-1}$, and the three absorbers with $W > 100 \text{ km s}^{-1}$ all have $\delta > 100$. The system that produces the strongest O VII and O VIII absorption has $\delta \sim 10^4$, but this system is weak in O VI because of its high temperature ($T \sim 2 \times 10^6 \text{ K}$). In Figures 13–16, special symbols mark the five systems with the strongest O VII absorption. The “same” absorber may have different density and temperature in different panels because of the optical depth weighting by the corresponding ionic species and because the velocity ranges defined in the different species may not be identical.

Figure 13 confirms the impression from Figures 11 and 12 that strong O VII and O VIII absorption arises in high density gas, more characteristic of virialized halos than connecting filaments.⁹ Strong O VI absorbers also tend to be fairly high overdensity, though there are some strong O VI systems with $\delta \sim 10 - 50$, and the highest overdensity absorbers tend to be weak in O VI because they are too hot. For each species, the strongest absorbers usually have temperatures fairly close to the value where the corresponding ionic abundance peaks in collisional equilibrium (see Figure 2), but there is a spread in temperature at every value of W , and for all three species there is a tail of

⁹The value of the “virial” overdensity is not very well defined, since different papers choose the virial radius in different fashion, but most definitions yield a local overdensity $\delta \sim 50 - 100$ at the virial boundary. For example, Navarro, Frenk, & White (1997) find $\delta \sim 125$ for Λ CDM at the radius where the mean interior density is 200 times the *critical* density and $\delta \sim 40$ at the radius where the mean interior density is 200 times the mean density. (See their figure 3. Their Λ CDM parameters, $\Omega_m = 0.25$, $h = 0.75$, and $\sigma_8 = 1.3$, are significantly different from ours, in a direction that produces denser halos.)

weaker, lower temperature, lower density absorbers for which photoionization plays an important role. Our conclusions about O VI agree with those of Cen et al. (2001) and Fang & Bryan (2001), in that collisional ionization dominates for the strongest absorbers but photoionization becomes important at slightly lower equivalent widths. Our conclusions about O VII and O VIII appear consistent with those of HGM, to the extent that we can compare them. The collisional equilibrium assumption used by FBC in their simulation analysis should be fairly accurate for the strongest O VII and O VIII absorbers, but it breaks down for the lower density absorbers associated with filamentary structures.

With sufficiently good data, it should be possible to measure absorption by multiple ionization stages of oxygen, or to obtain limits on the relative absorption by different species. Figure 14 shows the predicted correlations between O VII and O VIII equivalent widths (top), O VI and O VII (middle), and O VI and O VIII (bottom). There is some ambiguity in the definition of these correlations, since the threshold algorithm will, in general, choose somewhat different velocity ranges to mark the same absorber in different species, and in some cases there may be an absorber above threshold in one species but no corresponding absorber in the other. In Figure 14, crosses represent absorption in the velocity range defined by the ion on the abscissa, and squares represent absorption in the velocity range defined by the ion on the ordinate. In many cases, the absorbers defined in these two ways nearly coincide, so the square and cross are close to each other, but in some cases, especially in the O VIII vs. O VI panel, there are absorbers in one species with no obvious counterpart in the other.

The top panel shows a fairly good correlation between O VII and O VIII absorption, as one might expect on the basis of Figures 2 and 4: there are substantial ranges of temperature where both species have high fractional abundance, and in this regime the density of both species increases in proportion to the gas density. However, the spread in IGM temperatures does produce significant spread in the O VIII/O VII ratio. In particular, there are some strong O VII systems with relatively weak O VIII; these correspond to high density gas where the temperature is too low to produce substantial O VIII by collisional ionization.

The O VII vs. O VI diagram shows a tight core of points with a well defined correlation, tracing the underlying correlation of both species with density (see Figure 13). The strongest O VI absorbers tend to have strong associated O VII, which suggests that following up known O VI absorbers is a promising way to find O VII X-ray forest absorption. However, there are some strong O VI absorbers with weak O VII, corresponding to dense, relatively cool gas in which lower ionization species dominate. Moreover, the strong O VII absorbers ($W \gtrsim 30 \text{ km s}^{-1}$) have a wide range of O VI strength, including quite low values, since the O VI fraction drops to nearly zero once the temperature exceeds $5 \times 10^5 \text{ K}$. Thus, while O VI is a useful signpost for O VII absorption, it will not mark the positions of all or even most strong O VII absorbers, nor should the existence of strong O VI absorption with weak O VII come as a surprise.

Despite the correlations between O VI and O VII and O VII and O VIII, there is virtually no

correlation between O VI and O VIII; the variations in temperature at fixed density that produce much of the scatter in the top two panels drive the O VIII/O VII and O VI/O VII ratios in opposite directions. The lack of correlation in the bottom panel is not surprising in light of Figure 2 and 4, which show only narrow ranges of temperature for which O VI and O VIII both have substantial fractional abundance.

Figure 15 displays these predictions in a form that is useful for interpreting X-ray forest searches at the redshifts of known O VI absorbers. Upper panels show the distributions of O VII and O VIII equivalent widths for systems with O VI equivalent width above 30 km s^{-1} (103 mÅ). Both distributions are bimodal, with a main peak of cooler systems that have weak O VII or O VIII and a secondary peak of hotter systems that have stronger X-ray absorption. Lower panels show the corresponding distributions for an O VI equivalent width threshold of 10 km s^{-1} (34 mÅ). Here the distributions are more dominated by weak O VII and O VIII systems, though there is still a tail of stronger absorbers. Once again it is clear that following up strong O VI absorbers is a useful way of finding X-ray forest absorption, but that many O VI absorbers, especially the weaker ones, have little associated O VII or O VIII.

Figure 16 shows the predicted correlations of O VI, O VII, and O VIII equivalent width with H I (Ly α) equivalent width, where in all cases we take the velocity ranges defined by the H I absorbers. For O VI there is a tight correlation at low equivalent widths, reflecting the increase of both H I and O VI with density in photoionized gas. There is a spread of points towards higher O VI associated with shock-heated gas — raising the temperature always decreases the HI fraction at a given density, but it can increase the O VI fraction. At high equivalent widths the O VI–H I correlation flattens and spreads, but it remains the case that most of the strong O VI systems have strong associated H I, and vice versa.

There are hints of the same correlation present in the O VII–H I diagram, but in this case the scatter is considerably larger, and at the high equivalent width end (defined either by high H I or by high O VII) there is an enormous spread in O VII/H I, with essentially no discernible correlation. The O VIII–H I diagram shows no significant correlation or anti-correlation, except that the strongest H I systems all have O VIII absorption with $W > 10 \text{ km s}^{-1}$. Given the radically different temperature ranges required for H I and O VIII to exist in substantial abundances, it seems likely that the H I absorption is arising in the environs of the hotter gas producing the O VIII absorption, rather than in the same gas. Unfortunately, the large spread in O VIII/H I and O VII/H I suggests that it will be difficult to infer the metallicity of X-ray forest systems directly from line ratios. The prospects are better for inferring the metallicity in O VI absorption systems, but these trace only the cooler portions of the forest.

5. Discussion

The advent of X-ray telescopes with large effective areas and instruments for high resolution spectroscopy opens a new window on the intergalactic medium, one that could reveal a large reservoir of previously hidden baryons. We have used a hydrodynamic simulation of the Λ CDM cosmological model to predict the properties of the X-ray forest at $z = 0$. In agreement with previous studies based on numerical simulations (HGM; FBC) and analytic methods (Perna & Loeb 1998; Fang & Canizares 2000), we find that the oxygen species O VII and O VIII produce the strongest X-ray forest lines, thanks to the high cosmic abundance of oxygen, the oscillator strengths of the transitions at 21.60Å (O VII) and 18.97Å (O VIII), and the relatively frequent occurrence of temperature and density regimes where these species have large fractional abundance. If the IGM metallicity at these temperatures and densities is $Z = 0.1Z_{\odot}$, as we assume in most of our calculations, then O VII and O VIII are the only X-ray forest lines likely to be detectable with existing instruments, and even these will be difficult to study in any comprehensive fashion. Other promising lines for study with future instruments include the helium-like and hydrogen-like species of carbon, nitrogen, and neon (C V, C VI, N VI, N VII, Ne IX, Ne X), Fe XVII, which has lower abundance but a large oscillator strength, and possibly Si XIII. We have not examined highly ionized species like Fe XXV and Fe XXVI, which occur only at high temperatures that are poorly represented in our $50h^{-1}\text{Mpc}$ box (see Fang & Canizares 2000 for analytic predictions).

Our conclusions about the detectability of these X-ray forest lines are summarized by the rightmost column of Table 1, which lists the equivalent width threshold at which we predict one line per unit redshift, and Table 3, which gives approximate 5σ detection thresholds for observations with *Chandra*, *XMM-Newton*, *Constellation-X*, and *XEUS*, assuming 500 ksec exposures and the source spectrum of the X-ray bright quasar H1821+643 ($z = 0.297$). Target-of-opportunity searches that observe blazars in very high states could potentially reach lower equivalent width thresholds (Nicastro, private communication). The full distribution functions for absorber equivalent widths are shown in Figures 7–9. The largest uncertainty in the predictions is the unknown metallicity distribution of the IGM at the relevant temperatures and densities. This distribution can itself be predicted by tracking the dispersal of metals in cosmological simulations (as done by, e.g., HGM and Cen et al. 2001), but the uncertainties in the escape of metals from the galaxies themselves make these results quite uncertain. We predict a lower frequency of detectable X-ray forest lines than FBC, mainly because we assume $Z = 0.1Z_{\odot}$ instead of the higher metallicity found in the central regions of hot X-ray clusters. For the same metallicity, the two simulations give similar predictions for the number of strong O VII absorbers, though the inclusion of radiative cooling and photoionization in our calculations tends to reduce the column densities of the strongest systems and substantially increase the number of weak absorbers. Our predicted O VII equivalent width distribution agrees with that of HGM at low W but falls below it at high W , perhaps because of differences in the assumed cosmological parameters and in the simulation methods, but perhaps because their strongest absorbers arise in regions of higher than average metallicity.

Our assumption of a uniform metallicity of $0.1Z_{\odot}$ with solar abundance ratios (instead of

the α -enhanced ratios characteristic of Type II SN enrichment) is probably conservative, and perhaps unduly pessimistic. The predicted equivalent width thresholds in Table 1 are approximately proportional to the assumed metallicity, except that they grow more slowly for $W \gtrsim 80 \text{ km s}^{-1}$ as saturation becomes significant (see Figure 6). As shown in Figure 7, the predicted number of systems at high equivalent width is sensitive to the scatter in IGM metallicity as well as its mean value. For example, if we include 0.4 dex of scatter about 0.1 solar metallicity, then the O VII and O VIII equivalent width thresholds corresponding to one line per unit redshift are about a factor of two higher than the values quoted in Table 1. Because the intrinsic equivalent width distribution is steep, the first X-ray forest systems to be detected are likely to lie on the high tail of the IGM metallicity distribution.

We have devoted much of our attention to the physical state of the gas producing O VII and O VIII absorption, as illustrated in Figures 11–16, especially Figure 13. Strong O VII and O VIII absorbers, with $W > 50 \text{ km s}^{-1}$, arise mainly in gas with $\delta \gtrsim 100$ and temperature $T \sim 10^{5.5} \text{ K} - 10^{6.5} \text{ K}$, where collisional ionization dominates over photoionization. Weaker absorbers arise in lower density gas ($\delta \sim 30$ for $W \sim 20 \text{ km s}^{-1}$) over a wider range of temperatures, with photoionization often playing a significant role. For $W > 10 \text{ km s}^{-1}$, all O VIII absorbers and most O VII absorbers arise in the temperature regime $10^5 \text{ K} < T < 10^7 \text{ K}$ identified by Cen & Ostriker (1999a) as the “warm-hot IGM,” which contains a substantial fraction of the low redshift baryons in cosmological simulations (Cen & Ostriker 1999a; Davé et al. 2001). However, one should keep in mind that the absorbers potentially detectable with *Chandra* or *XMM-Newton* trace only the high density regions of the WHIM, with overdensities characteristic of virialized groups rather than intergalactic filaments.

In agreement with Cen et al. (2001) and Fang & Bryan (2001), we find that the Λ CDM model can plausibly account for the high incidence of O VI (1032Å, 1038Å) absorbers at low redshift (Tripp & Savage 2000; Tripp, Savage, & Jenkins 2000; Savage et al. 2002), as shown in Figure 10. The O VI absorbers exhibit a well-defined trend between equivalent width and overdensity, though there are some extreme outliers (Figure 13). At every equivalent width there is a substantial range of gas temperatures (about a factor of ten), with photoionization dominating in the cooler systems. At $W \sim 20 \text{ km s}^{-1}$ ($\sim 70 \text{ mÅ}$), much of the O VI absorption arises in gas with overdensity $\delta \sim 10$.

In searches with *Chandra* or *XMM-Newton*, O VI absorbers will play a crucial role as signposts for O VII or O VIII absorption. If the IGM metallicity is $0.1 Z_\odot$, or even $0.3 Z_\odot$, then the predicted number of X-ray forest systems strong enough to be detected at the $\sim 5\sigma$ level needed in a “blind” survey is very small. However, if one is searching at the redshift of a known O VI system, then a $2 - 3\sigma$ detection is already significant, and the steepness of the equivalent width distribution translates a small change in detection threshold to a large change in predicted line density. H I Ly α absorption can also serve as a signpost, but the higher density of Ly α lines and the large scatter between H I and O VII or O VIII (Figure 16) makes it less useful for this purpose than O VI.

Recent observations provide several tentative detections of intergalactic O VII and O VIII

absorption. The most convincing detections are those of Nicastro et al. (2002), who find absorption features of O VII, O VIII, and Ne IX in their *Chandra* spectrum of PKS 2155-304, at wavelengths consistent with zero redshift. The implied O VII and O VIII column densities are $\sim 5 \times 10^{15} \text{ cm}^{-2}$. *XMM-Newton* and *Chandra* observations also show $z = 0$ absorption along lines of sight towards Mrk 421 and 3C 273 (Rasmussen, Kahn, & Paerels 2003; Fang, Sembach, & Canizares 2003). These observations suggest that highly ionized gas is fairly ubiquitous along lines of sight through the Local Group, as one might expect when looking out from a local maximum in the IGM density (see, e.g., Kravtsov, Klypin, & Hoffman 2002), though at least some of the absorption could be Galactic in origin (Fang, Sembach, & Canizares 2003). Our simulations predict that oxygen lines of this strength should be rare along random lines of sight beyond the Local Group (Fig. 7), and here the observational situation is more ambiguous. Fang et al. (2002b) find a statistically significant absorption feature in the *Chandra* spectrum of PKS 2155-304 that could correspond to O VIII absorption coincident with a known galaxy group at $cz = 16,600 \text{ km s}^{-1}$, with an implied column density $\sim 10^{16} \text{ cm}^{-2}$. However, the *XMM-Newton* spectrum appears to rule out the existence of an absorption feature at this level (Rasmussen, private communication; see Rasmussen, Kahn, & Paerels 2003). Mathur, Weinberg, & Chen (2003) use a *Chandra* spectrum of H1821+643 to search for absorption at the redshifts of previously known O VI systems (Tripp, Savage, & Jenkins 2000; Oegerle et al. 2000), obtaining apparent detections of one system in O VII and another in both O VII and O VIII. The statistical significance of the features is only $\sim 2\sigma$ in each case, but because the absorption redshifts are known *a priori* from the O VI measurements, the probability that they are simply noise fluctuations is small ($\sim 5\%$). The rest-frame equivalent widths are $\sim 150 \text{ km s}^{-1}$ and $\sim 110 \text{ km s}^{-1}$ for the O VII lines and $\sim 140 \text{ km s}^{-1}$ for the O VIII line, with corresponding column densities $\sim 3 - 4 \times 10^{15} \text{ cm}^{-2}$ (O VII) and $\sim 7 \times 10^{15} \text{ cm}^{-2}$ (O VIII), assuming no saturation. The existence of two such strong systems in a path length $\Delta z \sim 0.3$ is surprising relative to our predictions in Figure 7, unless the metallicity in these systems is substantially higher than 0.1 solar, though it is worth noting that this line of sight also has an unusually high incidence of O VI absorption (Oegerle et al. 2000; Tripp, Savage, & Jenkins 2000).

Further measurements of or limits on O VII and O VIII absorption associated with O VI will take us much further towards understanding this newly discovered population of low redshift O VI absorbers, providing constraints on their densities, temperatures, and ionization mechanisms and on their contribution to the cosmic baryon budget. However, O VI absorbers trace only the low temperature end of the X-ray forest; many strong O VII and O VIII systems have very weak O VI absorption, and, conversely, many strong O VI systems will be undetectable in O VII or O VIII (Figure 14). A full accounting of the strong O VII and O VIII absorbers will probably require a mission with the capabilities of *Constellation-X*, which may also begin to detect X-ray absorption from other elements in the same systems. Even at the $\sim 30 \text{ km s}^{-1}$ threshold of *Constellation-X*, the detectable X-ray forest absorbers at $Z = 0.1Z_{\odot}$ correspond mainly to gas in the outer regions of groups and poor clusters, with some contribution from more diffuse gas in filaments. The powerful *XEUS* satellite would allow a comprehensive investigation of X-ray forest absorption by a number of ionization species, providing great insight into the distribution of shock-heated baryons and the

enrichment of the intergalactic medium.

We are grateful to Smita Mathur for helpful advice at many stages in this work, especially in matters related to observational capabilities. We also thank Jordi Miralda-Escudé for several valuable discussions and Joop Schaye for comments on the manuscript. We thank Todd Tripp for providing the observational data points used in Figure 10 and Taotao Fang for providing the numerical results from Fang & Bryan (2001) and FBC (discussed in §3.1 and shown in Figure 10). This work was supported by NASA LTSA Grant NAG5-3525, NSF Grant AST-9802568, and Chandra Observatory Grant G01-2118X from Smithsonian Astrophysical Observatory. X.C. was supported at OSU by the Department of Energy under grant DE-FG02-91ER40690, and at ITP/UCSB by the NSF under grant PHY99-07949. D.W. acknowledges the hospitality of the Institute for Advanced Study and the financial support of the Ambrose Monell Foundation during the completion of this work. R.D. was supported by NASA through Hubble Fellowship grant number HST-HF-01128.01-A awarded by the Space Telescope Science Institute, which is operated by AURA, Inc., under NASA contract NAS5-26555. The simulation was performed at the San Diego Supercomputer Center and NCSA.

REFERENCES

Aguirre, A., Hernquist, L., Schaye, J., Katz, N., Weinberg, D. H., & Gardner, J. 2001, *ApJ*, 561, 521

Aurière, M. 1982, *A&A*, 109, 301

Aldcroft, T., Elvis, M., McDowell, J., & Fiore, F., 1994, *ApJ*, 437, 584

Barcons, X., & Fabian, A.C., 1992, *ARA&A*, 30, 429. (BF92)

Barlow, T. A. & Tytler, D., 1998, *AJ*, 115, 1725

Burles, S., & Tytler, D. 1997, *AJ*, 114, 1330

Burles, S., & Tytler, D. 1998, *ApJ*, 507, 732

Cen, R., Miralda-Escudé, J., Ostriker, J. P., & Rauch, M., 1994, *ApJ*, 427, L9

Cen, R. & Ostriker, J. P. 1999a, *ApJ*, 514, 1

Cen, R., & Ostriker, J. P., 1999b, *ApJ*, 519, L109

Cen, R., Tripp, T. M., Ostriker, J. P., & Jenkins, E. B. 2001, *ApJ*, 559, L5

Croft, R. A. C., Matteo, T. D., Davé, R., Hernquist, L., Katz, N., Fardal, M. A., & Weinberg, D. H., 2001, *ApJ*, 557, 67

Davé, R., Hellsten, U., Hernquist, L., Katz, N., & Weinberg, D. H. 1998, ApJ, 509, 661

Davé, R., Dubinski, J., & Hernquist, L., 1997, New Astronomy, 2, 71

Davé, R., Hernquist, L., Katz, N., and Weinberg, D. H., 1999, ApJ, 511, 521

Davé, R. et al. 2001, ApJ, 552, 473

de Bernardis, P. et al, 2002, ApJ, 564, 559

Ellison, S. L., Songaila, A., Schaye, J., & Pettini, M. 2000, AJ, 120, 1175

Fang, T. and Canizares, C. R., 2000, ApJ, 539, 532 (FC)

Fang, T. & Bryan, G. L. 2001, ApJ, 561, L31

Fang, T., Bryan, G. L., & Canizares, C. R. 2002a, ApJ, 564, 604 (FBC)

Fang, T., Marshall, H. L., Lee, J. C., Davis, D. S., & Canizares, C. R. 2002b, ApJ, 572, L127

Fang, T., Sembach, K. R., & Canizares, C. R. 2003, ApJ, 586, L49

Ferland, G. J., 1999, *Hazy, a Brief Introduction to Cloudy 94*, University of Kentucky, Physics Department Internal Report

Fiore, F., Nicastro, F., Savaglio, S., Stella, L., & Vietri, M., 2000, ApJ, 544, L7

Fukugita, M., Hogan, C. J., & Peebles, P. J. E., 1998, ApJ, 503, 518

Haehnelt, M. G., Steinmetz, M., & Rauch, M. 1996, ApJ, 465, L95

Hellsten, U., Gnedin, N. Y., & Miralda-Escudé, J., 1998, ApJ, 509, 56 (HGM)

Hellsten, U., Davé, R., Hernquist, L., Weinberg, D. H., & Katz, N. 1997, ApJ, 487, 482

Hernquist, L., & Katz, N. 1989, ApJS, 70, 419

Hernquist, L., Katz, N., Weinberg, D. H., & Miralda-Escudé, J., 1996, ApJ, 457, L51

Hui, L., & Gnedin, N. 1997, MNRAS, 292, 27

Hui, L., Gnedin, N. Y., & Zhang, Y., 1997, ApJ, 486, 599

Katz, N., Weinberg, D. H., & Hernquist, L., 1996, ApJS, 105, 19

Kravtsov, A. V., Klypin, A., & Hoffman, Y. 2002, ApJ, 571, 563

Mathur, S., Weinberg, D. H., & Chen, X. 2003, ApJ, 582, 82

Miyaji, T., Ishisaki, Y., Ogasaka, Y., Ueda, Y., Freyberg, M. J., Hasinger, G., & Tanaka, Y., 1998, A&A, 334, L13. (Mi98)

Miralda-Escudé, J., Cen, R., Ostriker, J. P., & Rauch, M., 1996, *ApJ*, 471, 582

Monaghan, J. J. & Lattanzio, J.C., 1985, *A&A*, 149, 135

Mushotzky, R. F., Loewenstein, M., Arnaud, K. A., Tamura, T., Fukazawa, Y., Matsushita, K., Kikuchi, K., & Hatsukade, I., 1996, *ApJ*, 466, 686

Navarro, J. F., Frenk, C. S., & White, S. D. M. 1997, *ApJ*, 490, 493

Nicastro, F. et al. 2002, *ApJ*, 573, 157

Oegerle, W. R. et al. 2000, *ApJ*, 538, L23.

Perna, R. & Loeb, A., 1998, *ApJ*, 503, L135

Phillips, L. A., Ostriker J. P., & Cen, R., 2001, *ApJ*, 544, L9

Pradhan, A. K., 2000, *ApJ*, 545, L165

Press, W. H., & Schechter, P. 1974, *ApJ*, 187, 425

Rasmussen, A., Kahn, S. M., & Paerels, F. 2003, to appear in The IGM/Galaxy Connection: The Distribution of Baryons at $z = 0$, (Kluwer: Dordrecht), astro-ph/0301183

Rauch, M., & Haehnelt, M. G. 1995, *MNRAS*, 275, L76

Rauch, M., Miralda-Escudé, J., Sargent, W. L. W., Barlow, T., Hernquist, L., Weinberg, D. H., Katz, N., Cen, R., & Ostriker, J. P., 1997, *ApJ*, 489, 7

Savage, B. D., Sembach, K. R., Tripp, T. M., & Richter, P., 2002, *ApJ*, 564, 631

Schaye, J., Rauch, M., Sargent, W. L. W., & Kim, T. 2000, *ApJ*, 541, L1

Schaye, J. 2001, *ApJ*, 559, 507

Shapiro, P. R. & Bahcall, J. N., 1980, *ApJ*, 241, 1

Shull, J. M., Roberts, D., Giroux, M. L., Penton, S. V., & Fardal, M. A. 1999, *AJ*, 118, 1450

Songaila, A., & Cowie, L. L., 1996, *AJ*, 112, 839

Spergel, D. N. et al. 2003, *ApJ*, submitted, astro-ph/0302209

Theuns, T., Leonard, A., Efstathiou, G., Pearce, F. R., & Thomas, P. A. 1998, *MNRAS*, 301, 478

Tripp, T. M. and Savage, B. D., 2000, *ApJ*, 542, 42

Tripp, T. M., Savage, B. D., & Jenkins, E. B., 2000, *ApJ*, 534, L1

Tripp, T. M., Giroux, M. L., Stocke, J. T., Tumlinson, J., & Oegerle, W. R., 2001, *ApJ*, 563, 724

Verner, D. A., Verner, E. M., & Ferland, G. J., 1996, *Atomic Data Nucl. Data Tables*, 64, 1

Weinberg, D. H., Hernquist, L., & Katz, N. 1997a, *ApJ*, 477, 8

Weinberg, D.H., Miralda-Escudé, J., Hernquist, L., & Katz, N., 1997b, *ApJ*, 490, 564

Zhang, Y., Anninos, P. & Norman, M. L., 1995, *ApJ*, 453, L57

Table 1: **Ions and their strongest transition lines**

Ion	E (keV)	λ (Å)	f	$10^5 Z/H$	W_1 (km s $^{-1}$)
C V	0.3079	40.27	0.65	35.5	18
C VI	0.3675	33.73	0.42	35.5	13
N VI	0.4307	28.79	0.68	9.33	5
N VII	0.5003	24.78	0.42	9.33	2.5
O VII	0.5740	21.60	0.70	74.1	40
O VIII	0.6536	18.97	0.42	74.1	25
Ne IX	0.9220	13.45	0.72	11.7	7
Ne X	1.022	12.13	0.42	11.7	3
Si XIII	1.865	6.648	0.76	3.55	2
Fe XVII	0.8257	15.02	3.0	3.24	8

Transitions producing the strongest X-ray forest absorption in our simulation. Columns 2-6 list the energy, wavelength, oscillator strength, element abundance by number relative to hydrogen for $Z = Z_\odot$, and the equivalent width threshold above which we find one line per unit redshift assuming $Z = 0.1Z_\odot$. Atomic data and abundances are from Verner, Verner, & Ferland (1996).

Table 2: **Instrument properties: spectral resolution and effective area**

		0.3keV(41Å)	0.5keV(25Å)	1keV(12Å)	2keV(6Å)	6keV(2Å)
Chandra ¹	R	1000		500	250	120
	A	8		25	60	100
XMM-Newton ²	R	800		500	250	120
	A	30		70	70	20
Constellation-X ³	R	800		500	300	1000
	A	1000		3000	15000	9000
XEUS ⁴	R	700		800	1000	1000
	A	30000		40000	40000	30000

All effective areas are given in cm 2 , – indicates no response.

¹ using LETG ACIS, grating 1st order.

² using RGS, grating 1st order.

³ design goal.

⁴ using STJ, design goal, initial mirror configuration.

Table 3: **Equivalent Width Thresholds for 5σ Detection**

		0.3keV(41Å)	0.5keV(25Å)	1keV(12Å)	2keV(6Å)	6keV(2Å)
Chandra	eV	0.24	0.45	1.3	4.7	< 72
	km/s	240	270	390	700	< 2600
	mÅ	33	22	16	15	< 18
XMM-Newton	eV	0.14	0.27	1.2	10	-
	km/s	140	160	360	1600	-
	mÅ	19	13	15	32	-
Constellation-X	eV	0.024	0.041	0.076	0.17	0.76
	km/s	24	25	23	26	38
	mÅ	3.3	2.0	0.94	0.53	0.26
XEUS	eV	0.0047	0.0089	0.025	0.094	0.59
	km/s	4.7	5.3	7.6	14	29
	mÅ	0.64	0.44	0.31	0.29	0.20

Equivalent widths corresponding to $S/N = 5$, computed from eq. (11) using the resolution and effective area values of Table 2, a 500 ksec integration time, and a quasar spectrum $F = 2 \times 10^{-3}(E/\text{keV})^{-2.35}$ photons $\text{cm}^{-2} \text{s}^{-1} \text{keV}^{-1}$ similar to that of the $z = 0.297$ quasar H1821+643.

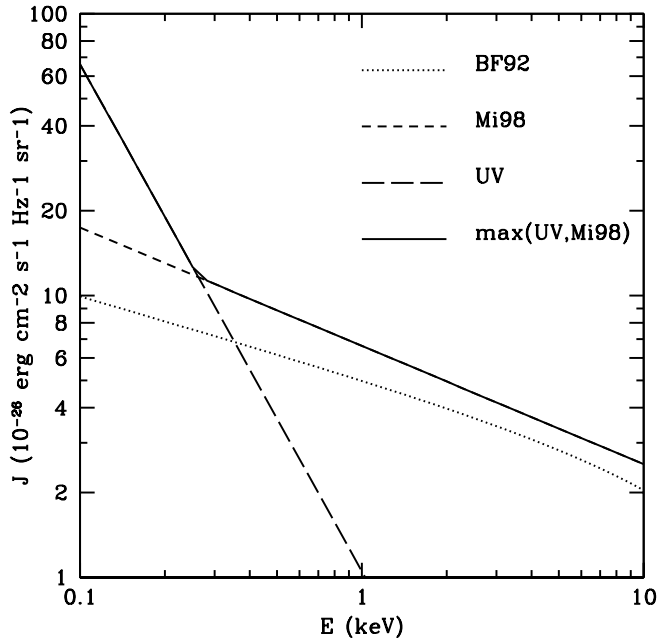


Fig. 1.— The X-ray and UV background spectra used in our calculations. The dotted line shows the BF92 spectrum, eq. (2). The short-dashed line, largely obscured by the solid line, shows the Mi98 spectrum, eq. (1). The long-dashed line shows the UV background spectrum of eq. (3), based on Shull et al. (1999). For most calculations, we take the maximum of the UV and Mi98 spectra, as shown by the solid line. For calculations involving oxygen ions, we also performed calculations with the BF92 spectrum for comparison.

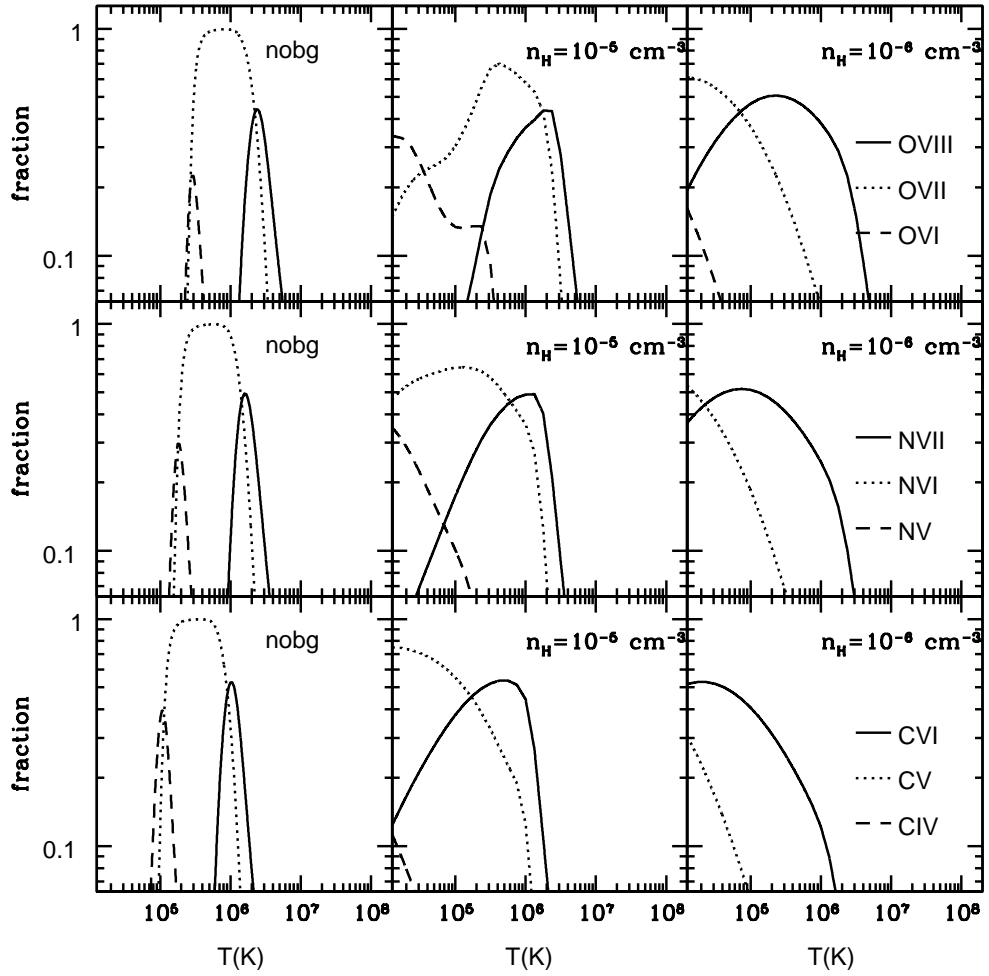


Fig. 2.— Ionization fractions of oxygen (top row), nitrogen (middle row), and carbon (bottom row) as a function of temperature. Left-hand panels show collisional ionization only. Central and right-hand panels show ionization fractions including photoionization by our standard X-ray + UV background (solid line of Fig. 1), for densities $n_H = 10^{-5} \text{ cm}^{-3}$ ($\delta = 60$) and $n_H = 10^{-6} \text{ cm}^{-3}$ ($\delta = 6$), respectively.

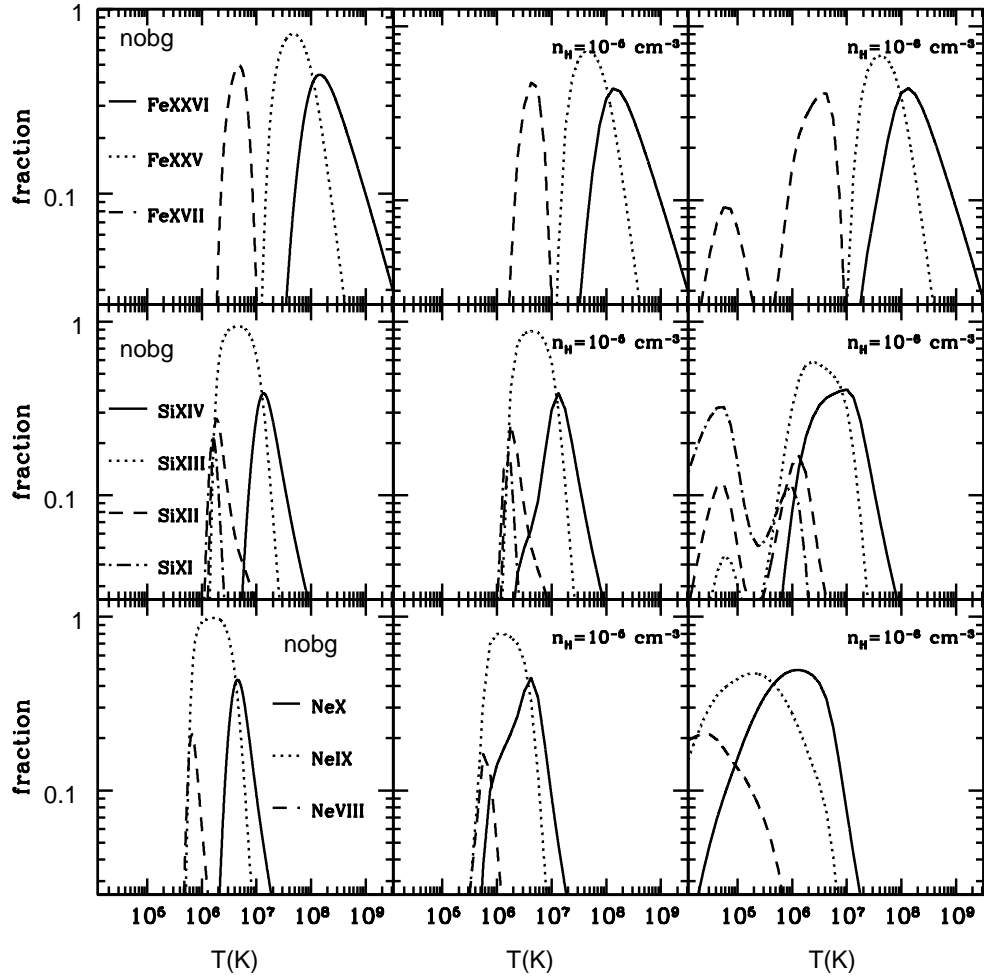


Fig. 3.— Like Fig. 2, but for iron (top row), silicon (middle row), and neon (bottom row). Note the expanded temperature scale relative to Fig. 2.

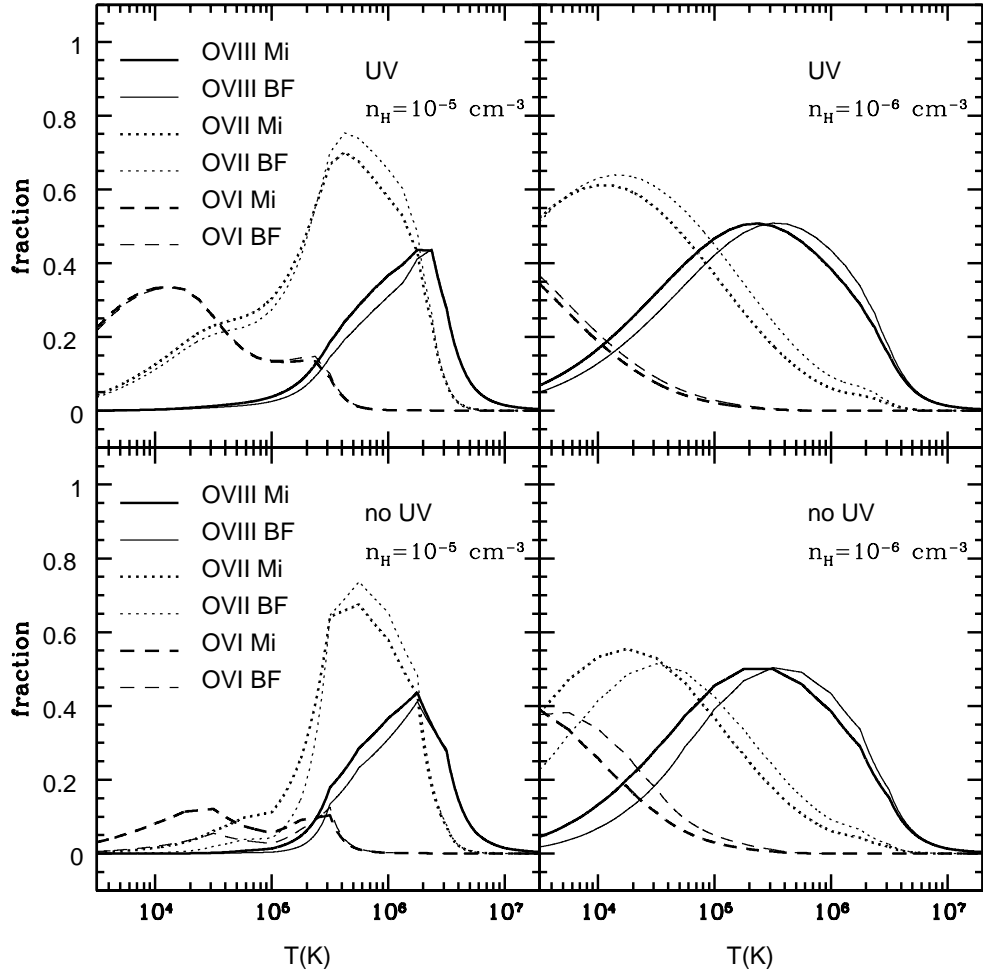


Fig. 4.— Influence of the background radiation on the O VI, O VII, and O VIII fractions. In the upper panels, heavy curves show our standard background, Mi98+UV, as in Fig. 2, for densities $n_H = 10^{-5} \text{ cm}^{-3}$ (left) and $n_H = 10^{-6} \text{ cm}^{-3}$ (right). (Relative to Fig. 2, note the use of a linear vertical scale and the extension to lower temperatures.) Light lines show results for the BF92 background instead of Mi98. Lower panels show the effect of omitting the UV background (but extrapolating the Mi98 or BF92 spectrum into the UV regime), which significantly reduces the O VI and O VII fractions at low temperatures for $n_H = 10^{-5} \text{ cm}^{-3}$.

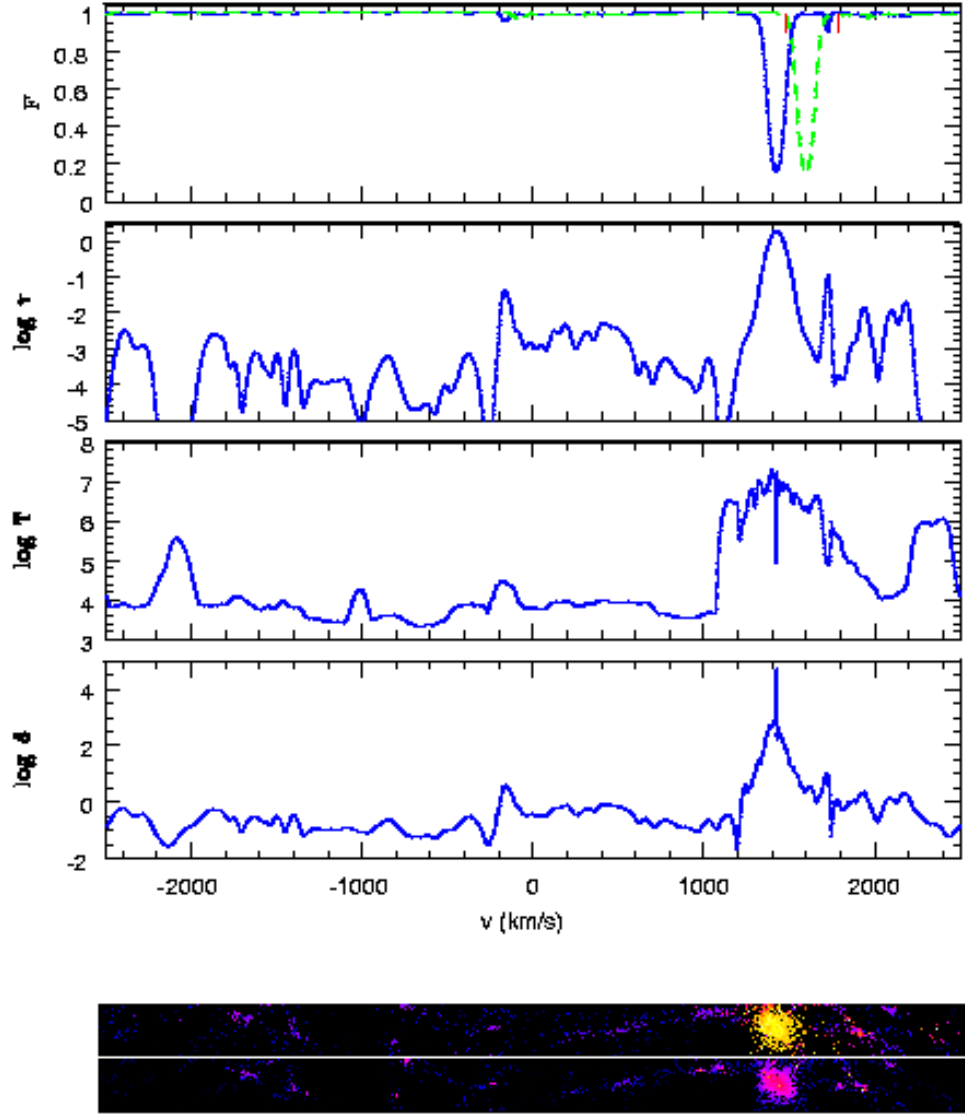


Fig. 5.— A Simulated spectrum for a line of sight with a strong O VII absorber. From top to bottom the panels show flux, optical depth, temperature and overdensity along the line of sight, as a function of spatial position expressed in velocity coordinates. The two strips at the bottom show the gas particles from the simulation in a rectangular prism $1h^{-1}\text{Mpc} \times 1h^{-1}\text{Mpc} \times 50h^{-1}\text{Mpc}$ centered on this line of sight, color coded by temperature (above) and density (below) (the color scheme is the same as that of Fig. 11). Solid curves in all panels are calculated in real space (no peculiar velocities) to allow the unambiguous identification of features from panel to panel. In the flux panel, the dashed line shows the redshift space spectrum, and ticks mark the region identified by our threshold algorithm as an “absorber” in the redshift space spectrum.

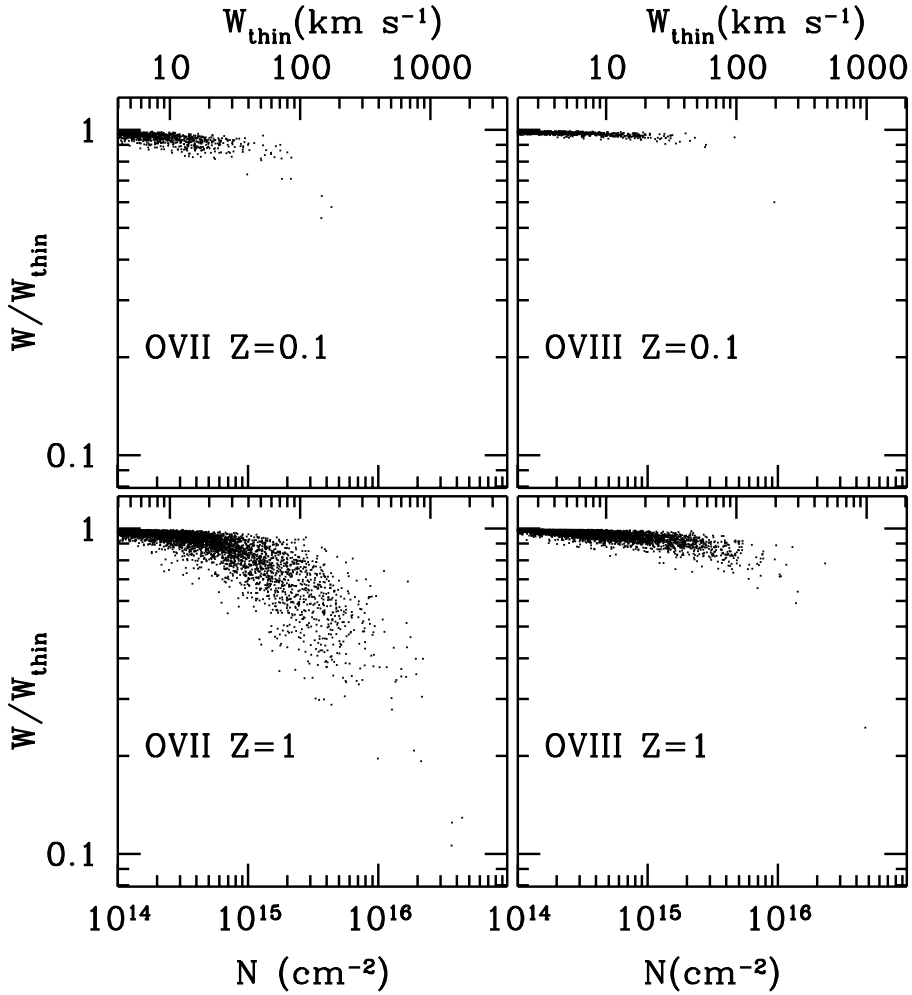


Fig. 6.— The ratio of the equivalent width of absorbers to the optically thin equivalent width, as a function of column density, for the O VII (left) and O VIII (right) absorbers along 1200 lines of sight through our simulation volume. The top panels are based on our standard metallicity assumption $Z = 0.1Z_{\odot}$, while the bottom panels assume a solar metallicity and are thus a factor of ten higher in column density. We plot W/W_{thin} , where $W_{\text{thin}} = 3.985(N/10^{14} \text{ cm}^{-2}) \text{ km s}^{-1}$ for O VII and $W_{\text{thin}} = 2.092(N/10^{14} \text{ cm}^{-2}) \text{ km s}^{-1}$ for O VIII. The upper axis label shows the value of W_{thin} corresponding to each column density.

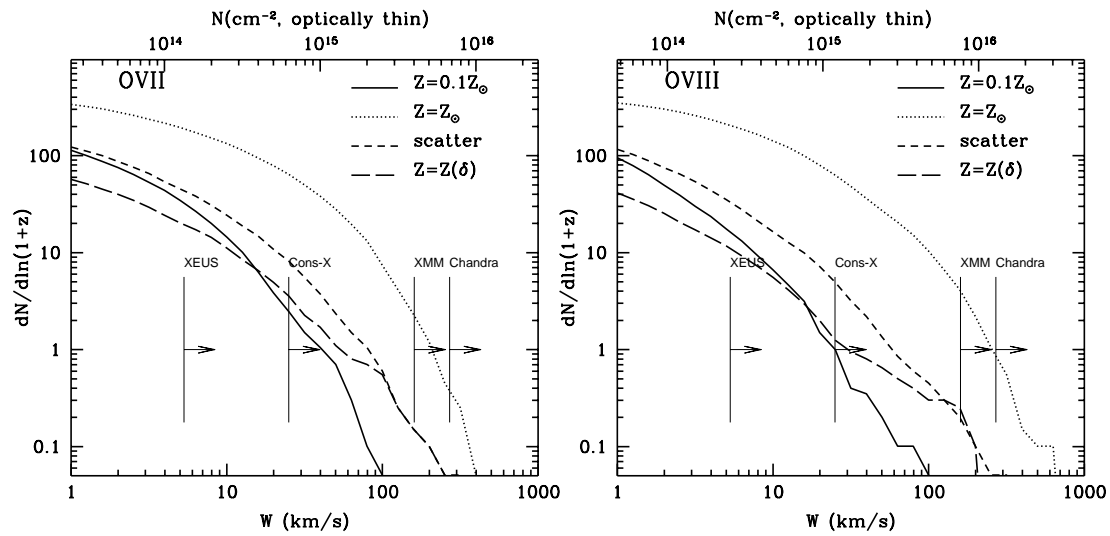


Fig. 7.— The cumulative distribution function of O VII (left) and O VIII (right) equivalent widths, i.e., the number of lines per unit redshift with equivalent width greater than W , computed at $z = 0$. On the top of each panel, we mark column densities corresponding to the given W values for an optically thin absorber (eq. 10); above $N \sim 2 \times 10^{15} \text{ cm}^{-2}$ these are lower than the true column densities (see Fig. 6). All curves are calculated for the Mi98+UV background, but they are insensitive to this choice. Solid curves show our standard case, uniform metallicity $Z = 0.1Z_{\odot}$. Dotted curves show uniform metallicity $Z = Z_{\odot}$. Short-dashed curves show the effect of scatter in metallicity; the metallicity of each line of sight is drawn randomly from a log-normal distribution with $\langle \log Z/Z_{\odot} \rangle = -1$, $\sigma_{\log Z} = 0.4$. Long-dashed curves show a calculation with the same metallicity scatter and a trend of mean metallicity with gas overdensity — $\langle \log Z/Z_{\odot} \rangle = -1.66 + 0.36 \log \delta$ — as advocated by Cen & Ostriker (1999b). Vertical bars mark representative 5σ detection thresholds for different X-ray satellites (see discussion in §3.2).

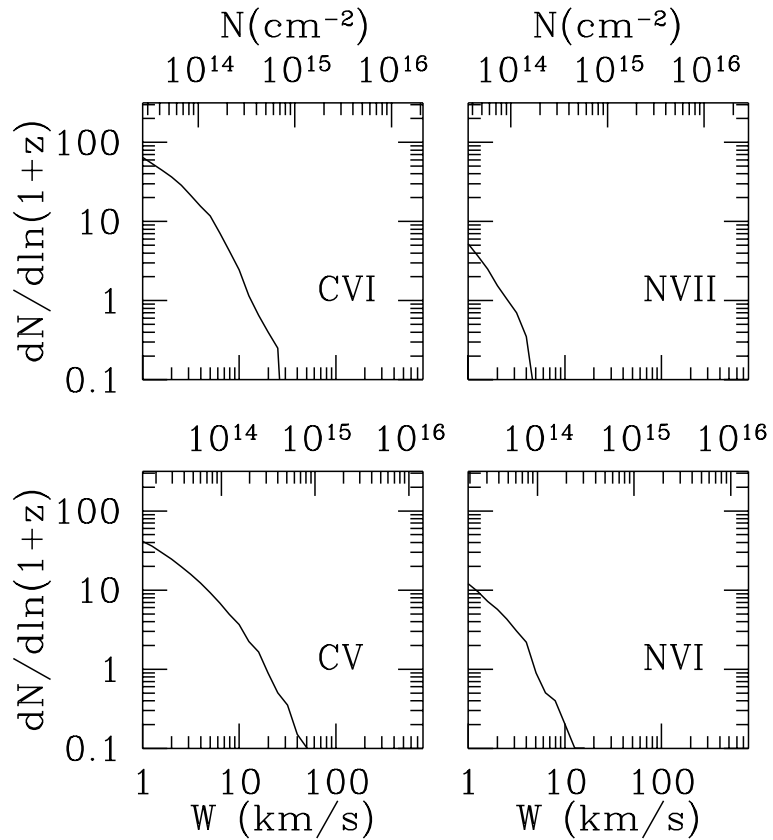


Fig. 8.— Cumulative equivalent width distributions of C V, C VI, N VI and N VII, computed assuming the Mi98+UV radiation background and $Z = 0.1Z_{\odot}$. The upper axis label shows the column density corresponding to the given equivalent width for an optically thin absorber.

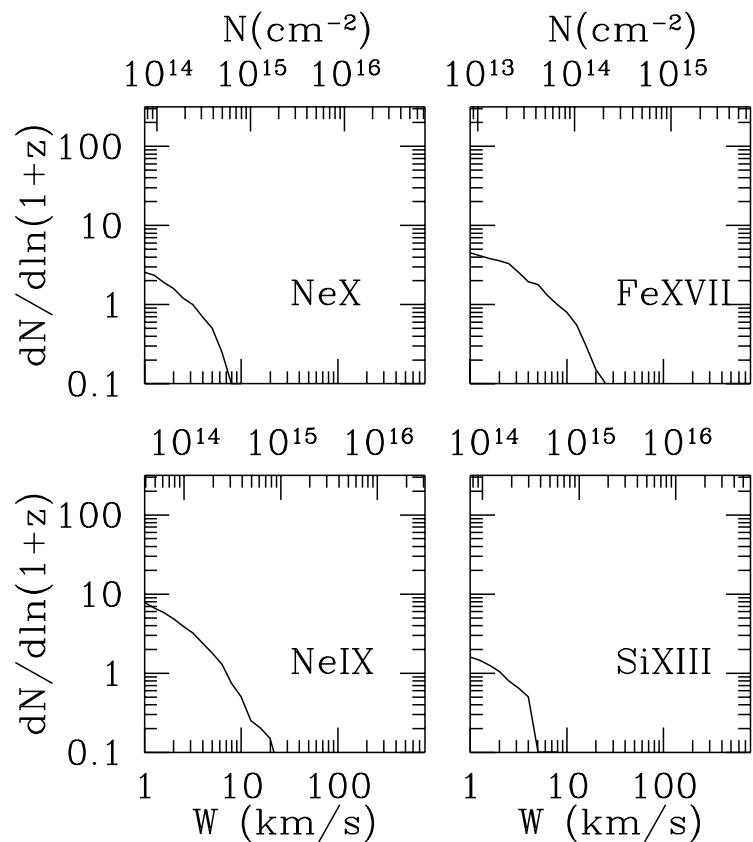


Fig. 9.— Like Fig. 8, but for Ne IX, Ne X, Si XIII and Fe XVII.

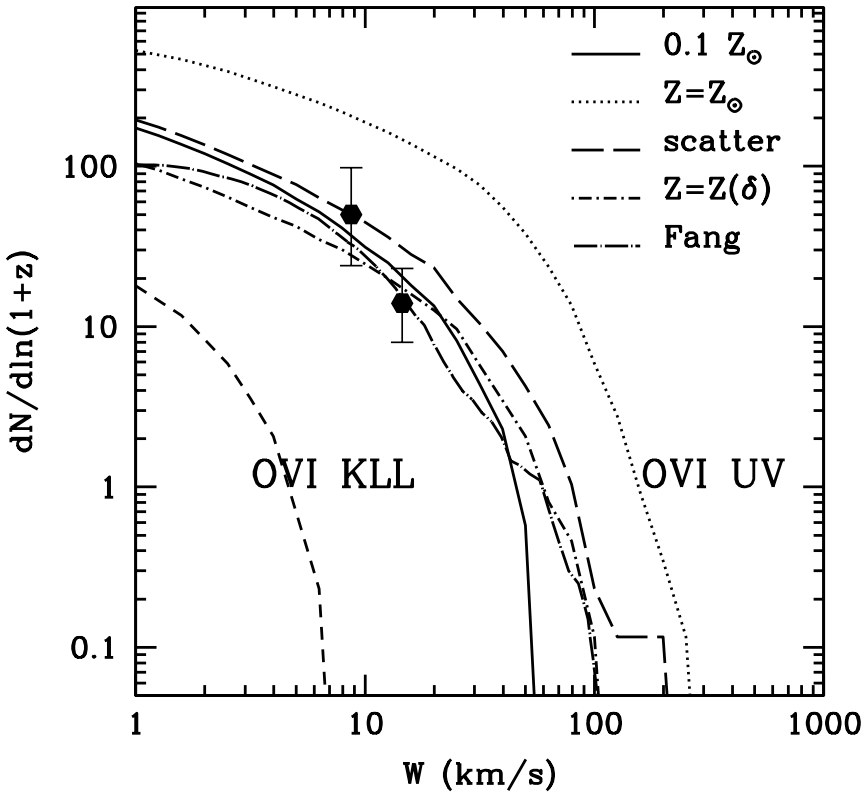


Fig. 10.— Cumulative equivalent width distribution of O VI absorbers, with a range of metallicity assumptions, all calculated for the Mi98+UV background. Solid and dotted curves show predictions for the 1032Å UV line, assuming uniform metallicity $Z = 0.1Z_{\odot}$ and $Z = Z_{\odot}$, respectively. Long-dashed and dot-short dashed curves show calculations with, respectively, metallicity scatter and a combination of metallicity scatter with density-dependent mean metallicity, as in Figure 7. The dot-long dashed curve shows the results of Fang & Bryan (2001), specifically their “Model B,” which incorporates photoionization; their metallicity model is closest to that of the $Z = Z(\delta)$ (dot-short dashed) curve above. Points with error bars show corresponding observational data from Tripp, Savage, & Jenkins (2000) and Savage et al. (2002), as taken from figure 2 of Cen et al. (2001). The short-dashed curve at lower left shows the equivalent width distribution of KLL resonance absorption in the X-ray, for $Z = 0.1Z_{\odot}$.

Fig. 11.— The gas particle distribution in a $25h^{-1}\text{Mpc} \times 25h^{-1}\text{Mpc} \times 25h^{-1}\text{Mpc}$ subvolume of our simulation, with particles color-coded by temperature (top left), density (top right), O VII ion fraction (bottom left) and O VIII ion fraction (bottom right). The temperature scale runs from $T \sim 10^{3.5}\text{ K}$ (blue) through $T \sim 10^5\text{ K}$ (red) to $T \sim 10^7\text{ K}$ (yellow). The density scale runs from $\delta \sim 100$ (blue) through $\delta \sim 5 \times 10^3$ (red) to $\delta \sim 5 \times 10^5$ (yellow). The ion fraction scales are linear and run from ~ 0.2 (blue) through ~ 0.5 (red) to ~ 0.85 (yellow).

Fig. 12.— The projected O VII column density through the $50h^{-1}\text{Mpc}$ simulation volume, which has a redshift depth $\Delta z = 0.0167$. The maps have thresholds of $\log N_{\text{OVII}}$ of 14 (top left), 14.5 (top right), 15 (bottom left), and 15.5 (bottom right), and are computed assuming a metallicity $Z = 0.1Z_{\odot}$. The last three panels correspond roughly to the detection thresholds for *XEUS*, *Constellation-X*, and *Chandra/XMM-Newton*. For an assumed metallicity of $Z = 0.3Z_{\odot}$, column densities would increase by 0.5 dex, so a similar identification would hold for the first three panels instead of the last three.

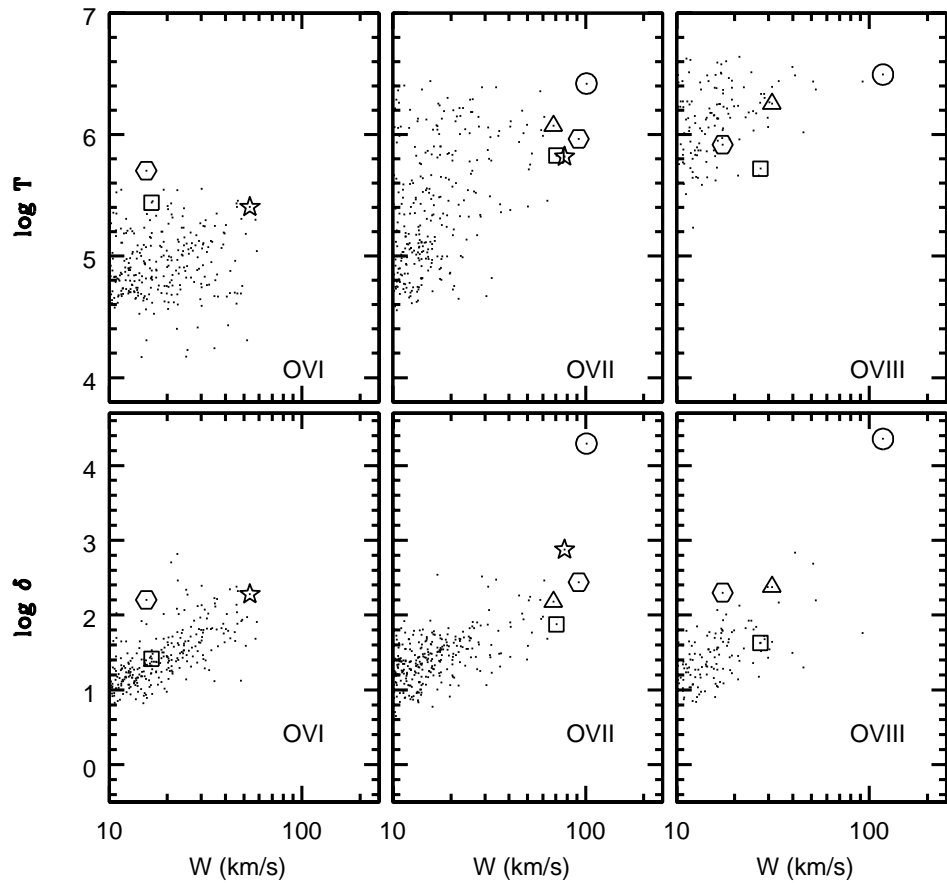


Fig. 13.— Temperature (top) and overdensity (bottom) of the gas associated with O VI, O VII, and O VIII absorbers, plotted against absorber equivalent width, for $Z = 0.1Z_{\odot}$. In this figure and the two that follow, the five systems with the strongest O VII absorption are marked with special symbols in each panel.

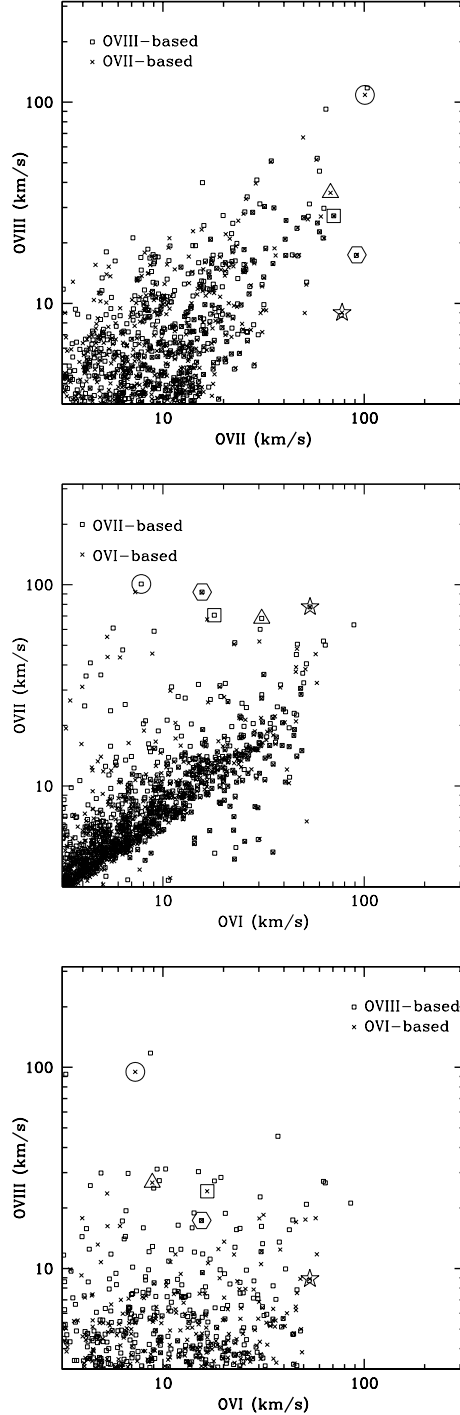


Fig. 14.— The equivalent width correlation for oxygen ions: O VII–O VIII (top), O VI–O VII (middle), O VI–O VIII (bottom). Different symbols denote absorber boundaries defined by the ion on the abscissa (crosses) or ordinate (squares). Large symbols mark the five systems with the strongest O VII absorption.

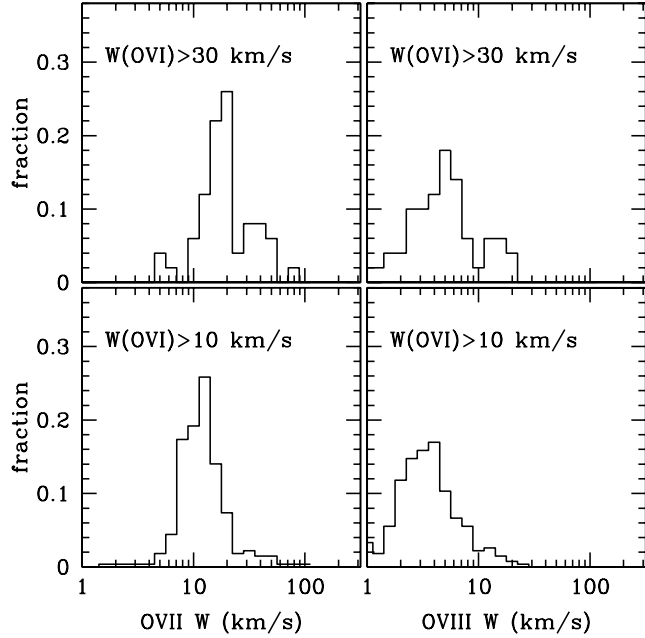


Fig. 15.— Histogram of O VII (left) and O VIII (right) equivalent widths for O VI absorbers with $W(O VI)$ greater than 30 km/s (top) and 10 km/s (bottom).

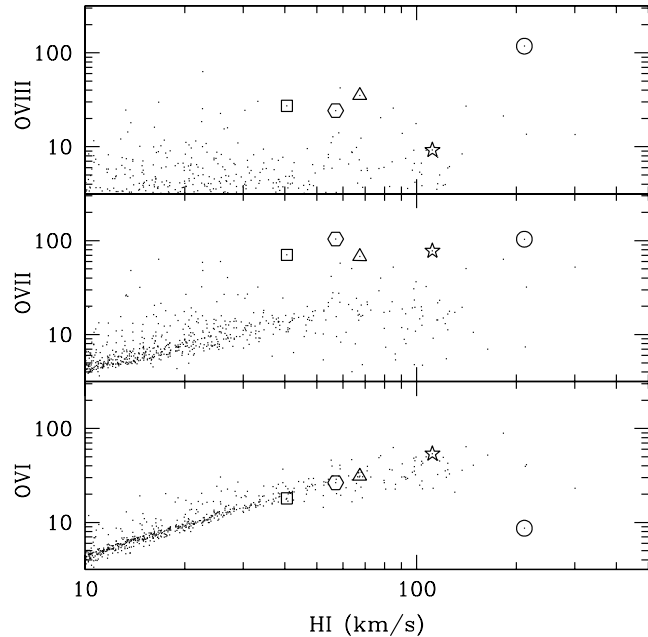


Fig. 16.— The correlation between H I and O VI, O VII, and O VIII equivalent width.

This figure "Fig11.jpg" is available in "jpg" format from:

<http://arxiv.org/ps/astro-ph/0203319v2>

This figure "Fig12.jpg" is available in "jpg" format from:

<http://arxiv.org/ps/astro-ph/0203319v2>